

NeurTV: Total Variation on the Neural Domain

Yisi Luo*, Xile Zhao†, Kai Ye‡, and Deyu Meng§

Abstract. Recently, we have witnessed the success of total variation (TV) for many imaging applications. However, traditional TV is defined on the original pixel domain, which limits its potential. In this work, we suggest a new TV regularization defined on the neural domain. Concretely, the discrete data is continuously and implicitly represented by a deep neural network (DNN), and we use the derivatives of DNN outputs w.r.t. input coordinates to capture local correlations of data. As compared with classical TV on the original domain, the proposed TV on the neural domain (termed NeurTV) enjoys two advantages. First, NeurTV is not limited to meshgrid but is suitable for both meshgrid and non-meshgrid data. Second, NeurTV can more exactly capture local correlations across data for any direction and any order of derivatives attributed to the implicit and continuous nature of neural domain. We theoretically reinterpret NeurTV under the variational approximation framework, which allows us to build the connection between classical TV and NeurTV and inspires us to develop variants (e.g., NeurTV with arbitrary resolution and space-variant NeurTV). Extensive numerical experiments with meshgrid data (e.g., color and hyperspectral images) and non-meshgrid data (e.g., point clouds and spatial transcriptomics) showcase the effectiveness of the proposed methods.

Key words. Total variation, deep neural network, continuous representation

MSC codes. 94A08, 68U10, 68T45

1. Introduction. Total variation (TV) regularization [42, 41] has been a very successful method for a wide range of imaging applications [23, 19, 31, 22]. The main aim of TV is to capture local correlations of data to reconstruct signals with degradations, e.g., signals with noise [12] or missing pixels [1]. Over the past decades, vast TV-based models were proposed to address the problems in many image processing problems, such as denoising [18], deblurring [4], deconvolution [8], unmixing [21], retinex [39], etc. Among these models, some representative regularization methods beyond the classical TV configuration were developed, such as the higher-order total generalized variation [5], directional total variation [3], weighted total variation [11, 50] and so on [7, 55, 19, 23, 22, 56]. These TV methods successfully address some limitations of the classical TV such as staircase effects [28], loss of contrast [41], and isotropy property [3]. Nowadays, TV has also been widely utilized in mainstream science fields, e.g., gene analysis [54], low-dose computed tomography [27], and seismic inversion [17], serving as a fundamental tool for many tasks in real life.

Classical TV regularizations are defined on the original pixel domain, which limits their potential in two aspects. First, the usage of classical TV is limited to meshgrid data such as images and is not suitable for emerging non-meshgrid data, e.g., point clouds and spatial transcriptomics [47], since it is difficult to define the discrete difference operator for non-meshgrid data. Second, the classical TV solely utilizes vertical and horizontal differences, which can

*School of Mathematics and Statistics, Xi'an Jiaotong University, Xi'an, China.

†School of Mathematical Sciences, University of Electronic Science and Technology of China, Chengdu, China.

‡School of Automation Science and Engineering, Faculty of Electronic and Information Engineering, Xi'an Jiaotong University, Xi'an, China.

§School of Mathematics and Statistics, Xi'an Jiaotong University, Xi'an, China.

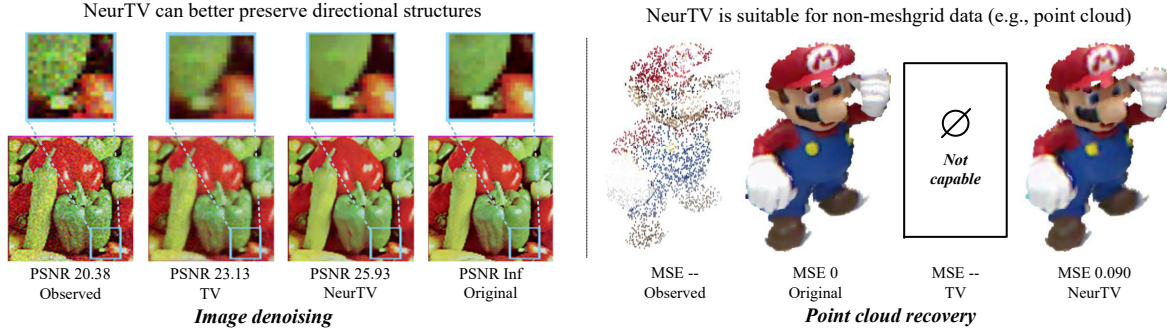


Figure 1. The results of image denoising on “Peppers” and the results of point cloud recovery on “Mario” by using classical TV and the proposed NeurTV. NeurTV is suitable for both meshgrid and non-meshgrid data (e.g., point cloud), while TV is not suitable for non-meshgrid data. Moreover, NeurTV can better capture directional features by using the directional derivatives of DNN in the continuous domain.

not sufficiently capture local correlations of data existed in more comprehensive directions and orders of derivatives. A remedy to enhance the flexibility of TV is to consider improved discretization schemes, e.g., by using multiple directional differences [16], second-order differences [5, 28], and learning adaptive discretizations from paired datasets [6]. However, these improved discretization methods rely on carefully designed discrete approximation operators, and hence their characterizations for directional and high-order derivatives are generally quite heuristic and complex.

In this work, we suggest a new TV regularization on the neural domain. Concretely, the discrete data (e.g., meshgrid data such as image and non-meshgrid data such as point cloud) is continuously and implicitly represented by a deep neural network (DNN), and we use the derivatives of DNN outputs w.r.t. input coordinates to capture local correlations of data. As compared with classical TV on the original pixel domain, the proposed TV on the neural domain (termed NeurTV) enjoys two advantages (as intuitively shown in Fig. 1). First, our NeurTV is not limited to meshgrid but is suitable for both meshgrid (e.g., image) and non-meshgrid (e.g., point cloud) data attributed to the continuous representation. Second, NeurTV can be readily extended to capture local correlations of data for any direction and any order of derivatives in a more accurate and concise manner than classical TV, since we can directly utilize the directional and higher-order derivatives of DNN without designing additional discrete difference operators.

To justify the proposed NeurTV, we reinterpret NeurTV from the variational approximation perspective, which allows us to build intrinsic connections between our NeurTV and classical TV regularizations. Specifically, we show that NeurTV and difference-based TV are closely related in the infinite condition, but are not equivalent in the finite condition, which rationally explains their performance gap. Moreover, the variational approximation motivates us to develop variants of NeurTV such as arbitrary resolution NeurTV based on the continuous representation, and space-variant NeurTV by designing spatially varying scale and directional parameters, which further improves the flexibility and effectiveness of NeurTV. Furthermore, NeurTV is flexibly integrated as a plug-and-play module, thereby allowing a wider range of potential applications. In this work, we consider multiple applications on and beyond meshgrid, including image denoising, inpainting, hyperspectral image mixed noise re-

removal (on meshgrid), point cloud recovery, and spatial transcriptomics reconstruction (beyond meshgrid), which are validated through a series of numerical experiments.

In summary, the contributions of this work are as follows.

- We propose the NeurTV regularization by using a DNN to continuously and implicitly represent data. Instead of using image differences on the pixel domain, we utilize the derivatives of DNN outputs w.r.t. input coordinates on the continuous neural domain to more comprehensively capture local correlations of data. Attributed to the continuous representation, NeurTV is suitable for both meshgrid and non-meshgrid data. Meanwhile, NeurTV can more exactly capture local correlations of data for any direction and any order of derivatives.
- We theoretically reinterpret NeurTV from the variational approximation perspective, which allows us to draw insightful connections between NeurTV and classical TV regularizations and also motivates us to develop more variants, e.g., arbitrary resolution NeurTV and space-variant NeurTV, which further improve the effectiveness and flexibility of NeurTV on its capability of capturing local correlations underlying data.
- The suggested NeurTV regularization constitutes a basic building block that allows a wide range of potential applications. Specifically, we consider different applications including image denoising, inpainting, hyperspectral image mixed noise removal (on meshgrid), point cloud recovery, and spatial transcriptomics reconstruction (non-meshgrid). Extensive numerical experiments demonstrate the effectiveness of our NeurTV regularization.

The rest of the paper is organized as follows. Sec. 2 introduces some related works. Sec. 3 presents the proposed NeurTV regularization and discusses its advantages and relations with classical TV. Moreover, we introduce some variants of NeurTV to more effectively capture local correlations of data. Sec. 4 conducts numerical experiments using meshgrid and non-meshgrid data to show the effectiveness of NeurTV. Sec. 5 finally concludes the study.

2. Related Works.

2.1. Interpolation and Rotation-based Methods. In the literature, some methods have attempted to enhance the flexibility of the TV from the perspective of interpolation or rotation [3, 40]. For example, Hosseini [16] considered interpolation to construct TV with four directions (i.e., horizontal, vertical, and two diagonal directions), which is a more effective discrete TV. Similarly, Zhuang et al. [59, 60] proposed the learned gradient prior by interpolating over a rectangle space to define directional derivatives. The well-known directional TV [3] can capture local directional smoothness of data by weighting the vertical and horizontal differences to create new directional differences beyond the meshgrid. Another type of directional TV is based on rotations. For instance, Jiang et al. [24] and Chang et al. [53] rotated the image and then performed TV regularization to depict directional information of specific patterns. Zhuang et al. [58] rotated the feature maps of a deep neural network and then performed the TV to implicitly model directional derivative information. The main aim of these methods is to characterize directional derivative information beyond meshgrid by using elaborately designed interpolation or rotation techniques. As compared, our NeurTV can more accurately and concisely capture local correlations of data for arbitrary directions by using derivatives of DNN in the continuous space. The proposed NeurTV does not need to

perform interpolation, rotation, or other operators to calculate directional derivatives. Hence NeurTV can be more conveniently extended to capture directional local correlations of data, which avoids the approximation process brought by interpolation and rotation.

2.2. Basis Function-based Methods. Another type of methods that related to this work are the basis function-based regularization methods [52, 10, 25, 20]. The pioneer works [52, 10] utilized basis functions (e.g., Gaussian basis [52]) to reveal the implicit smoothness between adjacent elements of the investigated matrix. Other basis functions such as Fourier series [25] or Chebyshev expansions [14] were also utilized to represent matrices/tensors in function representations, which tend to induce implicit smoothness brought from the continuous nature of function representation. The main aim of these basis function-based methods is to represent discrete meshgrid data via basis functions with adaptively learned coefficients to implicitly keep the local smoothness of the representation brought from the smoothness of basis functions. As compared with these methods, our NeurTV has two advantages. First, as compared with shallow basis functions, our NeurTV has stronger representation abilities brought from the DNN to characterize more complex structures underlying data. Second, our NeurTV can be readily extended to capture local correlations for any direction and any order of derivatives. Such explicit directional and higher-order derivatives-based local correlations, however, are relatively hard to be excavated by shallow basis function-based methods.

3. The Proposed Methods. In this section, we first introduce a general data recovery model by using the DNN to continuously represent data in Sec. 3.2. In Sec. 3.3, we introduce the proposed NeurTV regularization based on continuous representation and discuss its advantages over classical TV. In Sec. 3.5, we reinterpret NeurTV from the variational approximation perspective, which allows us to draw connections between NeurTV and classical TV and also motivates us to develop more variants of NeurTV, further improving its effectiveness.

3.1. Notations. We use $x, \mathbf{x}, \mathbf{X}, \mathcal{X}$ to denote scalar, vector, matrix, and tensor, respectively. The i -th element of a vector \mathbf{x} is denoted by $\mathbf{x}_{(i)}$. The (i_1, i_2, \dots, i_N) -th element of an N -th order tensor \mathcal{X} is denoted by $\mathcal{X}_{(i_1, i_2, \dots, i_N)}$. The notation $\mathbf{X}_{(i,:)}$ refers to the i -th row of the matrix \mathbf{X} , and it is similar for tensors. The discrete difference operator of a tensor $\mathcal{X} \in \mathbb{R}^{n_1 \times n_2 \times \dots \times n_N}$ along its d -th dimension ($d = 1, 2, \dots, N$) is denoted by $D_d \mathcal{X} := \mathcal{X}_{(:, \dots, 1:n_d-1, \dots, :)} - \mathcal{X}_{(:, \dots, 2:n_d, \dots, :)}$, which returns a tensor of size $n_1 \times \dots \times (n_d - 1) \times \dots \times n_N$. The ℓ_1 -norm of a tensor \mathcal{X} is denoted by $\|\mathcal{X}\|_{\ell_1} := \sum_{i_1, i_2, \dots, i_N} |\mathcal{X}_{(i_1, i_2, \dots, i_N)}|$. Given a differentiable multivariate function $f : \mathbb{R}^N \rightarrow \mathbb{R}$, the gradient operator is denoted by $\nabla f(\mathbf{x}) := (\frac{\partial f(\mathbf{x})}{\partial \mathbf{x}_{(1)}}, \frac{\partial f(\mathbf{x})}{\partial \mathbf{x}_{(2)}}, \dots, \frac{\partial f(\mathbf{x})}{\partial \mathbf{x}_{(N)}})^T$, which returns a vector containing partial derivatives along the N dimensions. Here for convenience we denote the partial derivative along the d -th dimension as $\nabla_d f(\mathbf{x}) := \frac{\partial f(\mathbf{x})}{\partial \mathbf{x}_{(d)}}$.

3.2. Data Recovery Model Based on Continuous Representation. TV is a widely-used regularization term for many imaging applications [41, 23, 22]. The traditional TV-based data recovery model [41, 39, 22] can be generally formulated as

$$(3.1) \quad \min_{\mathbf{X} \in \mathbb{R}^{n_1 \times n_2}} \text{Fidelity}(\mathbf{O}, \mathbf{X}) + \lambda \text{TV}(\mathbf{X}), \quad \text{TV}(\mathbf{X}) := \|D_1 \mathbf{X}\|_{\ell_1} + \|D_2 \mathbf{X}\|_{\ell_1},$$

where $\mathbf{O} \in \mathbb{R}^{n_1 \times n_2}$ denotes the observed matrix data. TV is defined by performing discrete differences between adjacent pixels of \mathbf{X} . As aforementioned, the classical TV has two potential shortcomings. First, it is not suitable for non-meshgrid data such as point cloud and spatial transcriptomics, since it is difficult to define difference operators for non-meshgrid data. Second, it is not flexible and accurate enough to capture local correlations of data for any direction and any order of derivatives.

To address these shortcomings, we propose a new regularization method, termed NeurTV regularization, based on the continuous representation using DNN. Our NeurTV regularization is suitable for both meshgrid and non-meshgrid data, and can be extended to more comprehensively capture local correlations of data for any direction and any order of derivatives more accurately. We first introduce the general data recovery model based on the continuous representation. Specifically, the discrete data can be seen as a point set sampled on a multivariate function defined in a continuous domain. Taking the image data as an example and denoting $\mathbf{O} \in \mathbb{R}^{n_1 \times n_2}$ as the observed image. We assume that the (i, j) -th element of \mathbf{O} is the function value of a function on the coordinate (i, j) , i.e., there exists a function $f : \Omega \rightarrow \mathbb{R}$ where $\Omega \subset \mathbb{R}^2$ such that $\mathbf{O}_{(i,j)} = f(i, j)$ holds for any i, j on the meshgrid. Then we can rationally reconstruct the signal by optimizing the function $f(\cdot)$ instead of the discrete matrix. Achieve an effective continuous representation needs to select a function $f(\cdot)$ with strong representation abilities [43, 45]. Inspired by recent continuous representation methods in deep learning [38, 9, 43], we propose to use a DNN to parameterize the continuous function $f(\cdot)$. A direct way to learn the underlying continuous representation of the discrete data \mathbf{O} is to optimize the following objective with a DNN $f_\Theta : \mathbb{R}^2 \rightarrow \mathbb{R}$ (where Θ denotes the DNN weights):

$$(3.2) \quad \min_{\Theta} \sum_{(i,j) \in \text{meshgrid}} (\mathbf{O}_{(i,j)} - f_\Theta(i, j))^2 + \lambda \Psi(\Theta),$$

where $\Psi(\Theta)$ denotes the regularization term conditioned on DNN parameters Θ for learning an effective continuous representation, and λ is a trade-off parameter. The first term in (3.2) is the fidelity term to keep the consistency between the observed data \mathbf{O} and the reconstructed signal using the continuous representation $f_\Theta(\cdot)$, and the second term is the regularization term for effective data recovery. As compared with traditional TV-based models for data recovery [41, 39, 22], our model (3.2) differs that we optimize the underlying continuous representation $f_\Theta(\cdot)$ instead of the discrete signal \mathbf{X} . This can help us to develop new regularization methods that tend to hold advantages delivered from the continuous representation.

In this work, we aim to design a regularization term to properly capture local correlations of data for general data recovery problems on and beyond meshgrid. For the image recovery tasks, the regularization for capturing local correlations of data can be simply set as the traditional discrete difference-based TV on meshgrid, i.e., by setting

$$(3.3) \quad \Psi(\Theta) = \sum_{(i,j) \in \text{meshgrid}} |f_\Theta(i+1, j) - f_\Theta(i, j)| + |f_\Theta(i, j+1) - f_\Theta(i, j)|.$$

However, for non-meshgrid data (e.g., point cloud), the observed points are not arranged on meshgrid, which makes discrete difference-based TV hard to apply.

To make the data recovery model (3.2) applicable for both meshgrid and non-meshgrid data, we reformulate the data recovery model as follows. First, the observed N -dimensional

discrete data can be stored in an n -by- $(N + 1)$ matrix $\mathbf{O} \in \mathbb{R}^{n \times (N+1)}$, where n denotes the number of observed points and N denotes the dimension number. For each $i = 1, 2, \dots, n$, $\mathbf{O}_{(i,:)}$ denotes the i -th observed point, where the first N elements of $\mathbf{O}_{(i,:)}$ (i.e., $\mathbf{O}_{(i,1:N)}$) contain the coordinates and the last element of $\mathbf{O}_{(i,:)}$ (i.e., $\mathbf{O}_{(i,N+1)}$) is the value at this coordinate. Using this notation, both meshgrid and non-meshgrid data can be uniformly represented and (3.2) can be formulated in a more general form by using an N -dimensional DNN $f_\Theta : \mathbb{R}^N \rightarrow \mathbb{R}$:

$$(3.4) \quad \min_{\Theta} \sum_{i=1}^n (\mathbf{O}_{(i,N+1)} - f_\Theta(\mathbf{O}_{(i,1:N)}))^2 + \lambda \Psi(\Theta).$$

In this new continuous representation model ((3.4)), the classical discrete difference-based TV can no longer be directly applied. Hence, it needs to develop a new regularization that can properly capture the local correlations of both meshgrid and non-meshgrid data under model (3.4). To meet this requirement, we propose the NeurTV regularization by using derivatives of DNN outputs w.r.t. input coordinates, which gets rid of the dependency on meshgrid¹.

3.3. Continuous Representation-based NeurTV. To construct an effective regularization term $\Psi(\Theta)$ in (3.4) to capture local correlations of both meshgrid and non-meshgrid data, we introduce the NeurTV regularization, which penalizes the derivatives of DNN outputs w.r.t. input coordinates to more sufficiently keep local smoothness of the continuous representation. Specifically, we introduce the following basic formulation of the NeurTV regularization.

Definition 3.1 (NeurTV). *Given a differentiable (w.r.t. both input \mathbf{x} and parameters Θ) function $f_\Theta : \Omega \rightarrow \mathbb{R}$ where $\Omega \subset \mathbb{R}^N$ and a point set $\Gamma \subset \Omega$, the NeurTV regularization conditioned on Θ is defined as*

$$(3.5) \quad \Psi_{\text{NeurTV}}(\Theta) := \sum_{d=1}^N \sum_{\mathbf{x} \in \Gamma} |\nabla_d f_\Theta(\mathbf{x})|.$$

By plugging this NeurTV regularization into the continuous representation-based data recovery model (3.4) we obtain the following model given the observed data \mathbf{O} :

$$(3.6) \quad \min_{\Theta} \sum_{i=1}^n (\mathbf{O}_{(i,N+1)} - f_\Theta(\mathbf{O}_{(i,1:N)}))^2 + \lambda \sum_{d=1}^N \sum_{\mathbf{x} \in \Gamma} |\nabla_d f_\Theta(\mathbf{x})|.$$

Here, the recovered discrete data can be obtained by querying $f_\Theta(\cdot)$ on discrete coordinates. Our NeurTV-based data recovery model (3.6) preserves the local smoothness of the recovered data by penalizing the local derivatives of DNN outputs w.r.t. inputs. Besides, our NeurTV-based model (3.6) has two advantages as compared with classical TV, as detailed below.

First, the NeurTV-based model (3.6) is not limited to be used on meshgrid data, but is suitable for both meshgrid and non-meshgrid data processing, e.g., image recovery and point cloud recovery. If the observed data \mathbf{O} represents meshgrid data, then the sampling set Γ

¹We remark that the data recovery models (3.2) & (3.4) can be readily tackled by standard gradient descent method by optimizing the parameters of DNN, and we consistently employ the Adam optimizer [26] to tackle the data recovery models presented in this paper.

could be set as meshgrid coordinates $\Gamma = \{(1, 1), (1, 2), \dots, (n_1, n_2)\}$. While if the observed data \mathbf{O} represents non-meshgrid data, then the sampling set Γ could be set as non-meshgrid coordinates. As compared, classical TV regularization is suitable for meshgrid data but can not be so directly and easily applied to non-meshgrid data like point cloud.

Second, our NeurTV can be more readily and exactly extended to capture local correlations of data for any direction and any order of derivatives. Specifically, classical TV-based methods need to develop more complicated discrete difference [5, 40, 7], interpolation [3, 59], or rotation operators [53, 24] to define directional or higher-order TV, since the original difference operators on meshgrid can not directly utilize directional and higher-order derivatives. These operators inevitably encounter approximation error issue when approximating directional or higher-order function derivatives. As compared, the proposed NeurTV can directly make use of directional and higher-order derivatives of DNN outputs w.r.t. inputs to more easily and concisely design directional or higher-order derivatives-based NeurTV. Next, we give the corresponding extensions of our NeurTV to directional and higher-order NeurTV regularizations.

3.4. Extensions of NeurTV. Our NeurTV can be easily extended to capture local correlations for any direction and any order of derivatives. In this section, we give some examples of the directional and higher-order derivatives-based NeurTV, including the directional NeurTV, the higher-order NeurTV, and the higher-order spatial-spectral NeurTV regularizations.

3.4.1. Directional NeurTV. The directional local correlations are beneficial for characterizing directional patterns beyond the vertical/horizontal directions. Traditionally, classical discrete meshgrid-based TV depends on image rotation [24] or interpolation [40] to define the directional TV, which are relatively too heuristic and complex. As compared, our NeurTV can be more easily extended to directional NeurTV by utilizing the directional derivative of DNN outputs w.r.t. inputs. Here, we take the two-dimensional case as an example.

Lemma 3.2. *Given a differentiable function $f : \Omega \rightarrow \mathbb{R}$ where $\Omega \subset \mathbb{R}^2$. The directional derivative along the direction $\mathbf{e} = (\cos \theta, \sin \theta)$ where $\theta \in [0, 2\pi)$ is defined as*

$$(3.7) \quad \nabla_{\mathbf{e}} f(\mathbf{x}) := \lim_{t \rightarrow 0^+} (f(\mathbf{x} + (t \cos \theta, t \sin \theta)) - f(\mathbf{x})) t^{-1}.$$

Such directional derivative of $f(\cdot)$ is equivalent to $\nabla_{\mathbf{e}} f(\mathbf{x}) = \nabla_1 f(\mathbf{x}) \cos \theta + \nabla_2 f(\mathbf{x}) \sin \theta$.

Proof. By using mid-value theorem, direct calculate yields

$$(3.8) \quad \begin{aligned} \nabla_{\mathbf{e}} f(\mathbf{x}) &= \lim_{t \rightarrow 0^+} (f(\mathbf{x} + (t \cos \theta, t \sin \theta)) - f(\mathbf{x})) t^{-1} \\ &= \lim_{t \rightarrow 0^+} (f(\mathbf{x} + (t \cos \theta, t \sin \theta)) - f(\mathbf{x} + (0, t \sin \theta))) t^{-1} \\ &\quad + \lim_{t \rightarrow 0^+} (f(\mathbf{x} + (0, t \sin \theta)) - f(\mathbf{x})) t^{-1} \\ &= \lim_{t \rightarrow 0^+} (\nabla_1 f(\xi) t \cos \theta) t^{-1} + \lim_{t \rightarrow 0^+} (\nabla_2 f(\eta) t \sin \theta) t^{-1}, \end{aligned}$$

where ξ and η satisfy $\lim_{t \rightarrow 0^+} \xi = \lim_{t \rightarrow 0^+} \eta = \mathbf{x}$. This then concludes that $\nabla_{\mathbf{e}} f(\mathbf{x}) = \nabla_1 f(\mathbf{x}) \cos \theta + \nabla_2 f(\mathbf{x}) \sin \theta$. ■

Definition 3.3 (Directional NeurTV). For a two-dimensional differentiable function $f_\Theta : \Omega \rightarrow \mathbb{R}$ parameterized by Θ where $\Omega \subset \mathbb{R}^2$, the directional NeurTV (NeurDTV) of $f_\Theta(\cdot)$ along the direction $\theta \in [0, 2\pi)$ is defined as

$$(3.9) \quad \Psi_{\text{NeurDTV}_\theta}(\Theta) = \sum_{\mathbf{x} \in \Gamma} (|\nabla_1 f_\Theta(\mathbf{x}) \cos \theta + \nabla_2 f_\Theta(\mathbf{x}) \sin \theta|),$$

where $\Gamma \subset \Omega$ is a point set sampled over the continuous space.

According to Lemma 3.2, the directional function derivative can be analytically performed along any direction of the two-dimensional continuous space. We can then naturally introduce the directional function derivative of DNN into the NeurTV regularization as shown in (3.9), which avoids the use of additional rotation or interpolation operators considered in classical directional TV-based methods [40, 24, 53]. Such directional NeurTV can more concisely and effectively characterize directional structures of data. In the first row of Fig. 2, we show the image denoising results by using TV, directional TV-based method [40], NeurTV, and the proposed NeurDTV regularization, which clearly show the superiority of our NeurDTV for capturing directional local correlations of data.

3.4.2. Higher-order NeurTV. Analogously, our NeurTV can be easily extended to higher-order NeurTV. Specifically, we can directly utilize higher-order derivatives of DNN, which avoids the discrete approximation process in classical higher-order TV-based methods [5, 7, 40, 28]. The higher-order NeurTV could ease the staircase effect [5, 28] induced by first-order methods. As a basic example, we consider the following second-order NeurTV regularization by taking the second-order derivatives of DNN.

Definition 3.4. For a two-dimensional second-order differentiable function $f_\Theta : \Omega \rightarrow \mathbb{R}$ where $\Omega \subset \mathbb{R}^2$, the second-order NeurTV of $f_\Theta(\cdot)$ is defined as

$$(3.10) \quad \Psi_{\text{2nd-NeurTV}}(\Theta) = \sum_{\mathbf{x} \in \Gamma} \left(\sum_{i=1}^2 |\nabla_i f_\Theta(\mathbf{x})| + \kappa \sum_{i,j=1}^2 |\nabla_i \nabla_j f_\Theta(\mathbf{x})| \right),$$

where $\Gamma \subset \Omega$ is a point set and κ is a trade-off constant.

The proposed second-order NeurTV regularization uses a weighted hybrid of the first-order and the second-order derivatives of the DNN $f_\Theta(\cdot)$ to convey local correlations underlying data. The use of second-order derivatives is expected to alleviate the staircase effect. To validate the effectiveness of our second-order NeurTV regularization, we show the image denoising results by using classical TV, higher-order TV-based method [40], NeurTV, and second-order NeurTV regularizations in the second row of Fig. 2. We can observe that the second-order NeurTV (3.10) obtains a better result than NeurTV. Especially, the second-order NeurTV evidently alleviates the staircase effect of the first-order NeurTV method.

3.4.3. Spatial-spectral NeurTV. Then, we introduce a new higher-order NeurTV regularization for multi-dimensional data. Specifically, we take the hyperspectral image (HSI) [49, 57] as an example. The HSI contains intrinsic structure of intense spatial-spectral local smoothness [2]. To represent the spatial-spectral local correlations of HSI, we propose the following second-order spatial-spectral NeurTV (termed NeurSSTV) regularization.

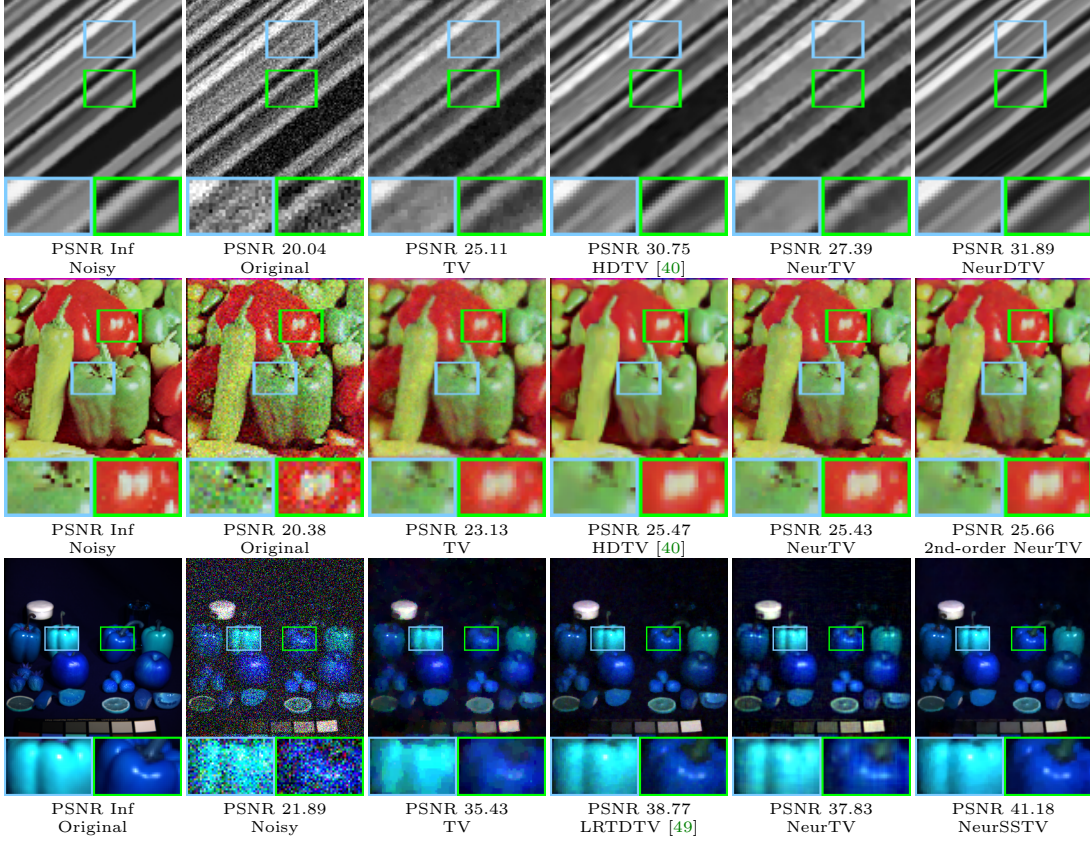


Figure 2. First row: The results of image denoising with Gaussian noise deviation 0.1 using the classical TV, the higher-order directional TV (HDTV) [40], the NeurTV, and the proposed directional NeurTV (3.9) (NeurDTV) with $\theta = -\frac{3\pi}{10}$. Second row: The results of image denoising with Gaussian noise deviation 0.1 using the classical TV, the HDTV, the NeurTV, and the proposed second-order NeurTV (3.10). Third row: The results of hyperspectral image denoising with Gaussian noise deviation 0.2 using the classical TV, the SSTV-based method LRTDTV [49], the NeurTV, and the proposed NeurSSTV (3.11).

Definition 3.5 (Spatial-spectral NeurTV). For a three-dimensional second-order differentiable function $f_\Theta : \Omega \rightarrow \mathbb{R}$ where $\Omega \subset \mathbb{R}^3$ (with the first two dimensions correspond to the spatial dimensions and the last dimension corresponds to the spectral dimension) and a point set $\Gamma \subset \Omega$, the NeurSSTV of $f_\Theta(\cdot)$ is defined as

$$(3.11) \quad \Psi_{\text{NeurSSTV}}(\Theta) = \sum_{\mathbf{x} \in \Gamma} (|\nabla_1 \nabla_3 f_\Theta(\mathbf{x})| + |\nabla_2 \nabla_3 f_\Theta(\mathbf{x})|),$$

where ∇_1, ∇_2 are two spatial partial derivative operators and ∇_3 is the partial derivative along the spectral dimension of the HSI.

The proposed NeurSSTV is defined by viewing the HSI as a three-dimensional differentiable function $f_\Theta(\cdot)$ parameterized by Θ . Different from the classical difference operators-based SSTV [2, 49], our NeurSSTV directly penalizes the higher-order derivatives of DNN. A numerical validation of our NeurSSTV as compared with the classical SSTV-based method [49] is shown in the third row of Fig. 2. It is obvious to observe that our NeurSSTV obtains

a better recovered result over the traditional SSTV [49], which validates the effectiveness of our NeurSSTV for multi-dimensional HSI recovery.

3.5. Justification of NeurTV from Variational Approximation. To further justify our NeurTV, we reinterpret NeurTV from the variational approximation perspective, which allows us to draw connections between NeurTV and classical TV and also motivates us to develop effective variants (i.e., arbitrary resolution NeurTV and space-variant NeurTV).

3.5.1. Reinterpretation of NeurTV. First, we introduce the functional TV [13], which is a variational regularization that penalizes the derivative of function anywhere.

Definition 3.6 (Total variation of function). *Given a function $f_\Theta : \Omega \rightarrow \mathbb{R}$ parameterized by Θ , where $\Omega \subset \mathbb{R}^N$, the TV of $f_\Theta(\cdot)$ in Ω is defined as*

$$(3.12) \quad V(f_\Theta; \Omega) := \sup \left\{ \int_{\Omega} f_\Theta(\mathbf{x}) \operatorname{div} \phi(\mathbf{x}) d\mathbf{x} : \phi \in C_c^\infty(\Omega, \mathbb{R}^N), \|\phi(\mathbf{x})\|_\infty \leq 1 \right\},$$

where div is the divergence operator and $\phi(\cdot)$ is a differentiable vector field with compact support.

This definition is valid for any integrable function $f_\Theta(\cdot)$ by considering the weak derivative concept. In this work, we can simply construct differentiable DNN $f_\Theta(\cdot)$ by stacking differentiable layers (e.g., choosing differentiable nonlinear activation function) and then calculate function derivative of DNN based on the chain rule. Hence we consider the following more familiar expression of functional TV by using function derivatives.

Lemma 3.7 (Total variation of differentiable function). *For a continuously differentiable function $f_\Theta : \Omega \rightarrow \mathbb{R}$ parameterized by Θ , its functional TV (3.12) equals to*

$$(3.13) \quad V(f_\Theta; \Omega) = \sum_{d=1}^N \int_{\Omega} |\nabla_d f_\Theta(\mathbf{x})| d\mathbf{x},$$

where ∇_d is the partial derivative along the d -th dimension.

Proof. By integration by parts, we have

$$(3.14) \quad \int_{\Omega} f_\Theta(\mathbf{x}) \operatorname{div} \phi(\mathbf{x}) d\mathbf{x} = \sum_{d=1}^N \int_{\Omega} f_\Theta(\mathbf{x}) \nabla_d \phi_d(\mathbf{x}) d\mathbf{x} = \sum_{d=1}^N \left(- \int_{\Omega} \nabla_d f_\Theta(\mathbf{x}) \phi_d(\mathbf{x}) d\mathbf{x} \right),$$

where ϕ_d denotes the d -th component of the vector field $\phi(\cdot)$. Here, the first term of integration by parts vanishes since $\phi(\cdot)$ has compact support and hence $\phi_d(\mathbf{x}) = 0$ for $\mathbf{x} \in \partial\Omega$. Since

$$(3.15) \quad - \int_{\Omega} \nabla_d f_\Theta(\mathbf{x}) \phi_d(\mathbf{x}) d\mathbf{x} \leq \int_{\Omega} |\nabla_d f_\Theta(\mathbf{x}) \phi_d(\mathbf{x})| d\mathbf{x} \leq \int_{\Omega} |\nabla_d f_\Theta(\mathbf{x})| d\mathbf{x}$$

and the equality attains when $\phi_d(\mathbf{x}) = -\nabla_d f_\Theta(\mathbf{x})/|\nabla_d f_\Theta(\mathbf{x})|$, we have

$$\begin{aligned}
V(f_\Theta; \Omega) &= \sup \left\{ \int_\Omega f_\Theta(\mathbf{x}) \operatorname{div} \phi(\mathbf{x}) d\mathbf{x} : \|\phi(\mathbf{x})\|_\infty \leq 1 \right\} \\
(3.16) \quad &= \sup \left\{ \sum_{d=1}^N \left(- \int_\Omega \nabla_d f_\Theta(\mathbf{x}) \phi_d(\mathbf{x}) d\mathbf{x} \right) : \|\phi(\mathbf{x})\|_\infty \leq 1 \right\} \\
&= \sum_{d=1}^N \int_\Omega |\nabla_d f_\Theta(\mathbf{x})| d\mathbf{x},
\end{aligned}$$

which completes the proof. ■

We can see that the TV of a differentiable function is the sum of integration of partial derivatives of the function. Recall that our NeurTV (3.5) is defined as the sum of the partial derivatives of DNN over a discrete set, and hence we can build connections between the functional TV (3.12) and our NeurTV by viewing the NeurTV as the numerical integration for approximating the variational regularization (3.12). Here, we consider uniformly sampled partitions in the one-dimensional case to study the variational approximation. The numerical integration in the one-dimensional case has the following form by taking quadratures:

$$(3.17) \quad V(f_\Theta; [a, b]) = \underbrace{\int_a^b |\nabla f_\Theta(x)| dx}_{\text{Functional TV}} \approx \underbrace{\sum_{i=2}^n |\nabla f_\Theta(x_i)|(x_i - x_{i-1})}_{\text{NeurTV}},$$

where $f_\Theta : \Omega \rightarrow \mathbb{R}$ is a differentiable function, $\Omega = [a, b] \subset \mathbb{R}$, and (x_1, \dots, x_n) are uniformly sampled partitions over $[a, b]$. Here, the interval $(x_i - x_{i-1})$ can be fused into the trade-off parameter λ in the NeurTV-based model (3.6). The following lemma shows that denser sampling (i.e., larger n) tends to let NeurTV be more accurate to approximate the functional TV $V(f_\Theta; [a, b])$, and the approximation is exact in the infinite condition, i.e., $n \rightarrow \infty$.

Lemma 3.8. *For a continuously differentiable function $f_\Theta : \Omega \rightarrow \mathbb{R}$ where $\Omega = [a, b] \subset \mathbb{R}$, we have*

$$(3.18) \quad V(f_\Theta; [a, b]) = \int_a^b |\nabla f_\Theta(x)| dx = \lim_{n \rightarrow \infty} \sum_{i=2}^n |\nabla f_\Theta(x_i)|(x_i - x_{i-1}),$$

where (x_1, \dots, x_n) are uniformly sampled partitions over $[a, b]$.

Proof. The first equality follows from Lemma 3.7 and the second equality follows from the definition of Riemann integration. ■

3.5.2. Connections Between Classical TV and NeurTV . Next, we draw connections between the proposed NeurTV and the classical difference operator-based TV. Specifically, the functional TV, $V(f_\Theta; [a, b])$, can also be approximated via difference operators without using the function derivatives, as stated below.

Lemma 3.9. *For a continuously differentiable function $f_\Theta : [a, b] \rightarrow \mathbb{R}$, its functional TV (3.12) equals to*

$$(3.19) \quad V(f_\Theta; [a, b]) = \int_a^b |\nabla f_\Theta(x)| dx = \sup_{\mathcal{P}} \left\{ \sum_{i=2}^n |f_\Theta(x_i) - f_\Theta(x_{i-1})| : n \in \mathbb{N}, \mathcal{P} = (x_1, \dots, x_n) \right\},$$

where \mathcal{P} are some partitions over $[a, b]$ with $x_1 = a$ and $x_n = b$.

Lemma 3.9 shows intrinsic relationship between the difference-based TV (i.e., the right term in (3.19)) and the functional TV. Here, the partitions \mathcal{P} can be taken non-uniformly. We have the following lemma which further shows the relation between the functional TV $V(f; [a, b])$ and the uniform partitions-based TV.

Lemma 3.10 (Total variation based on uniform partitions). *For a differentiable function $f_\Theta : [a, b] \rightarrow \mathbb{R}$, we consider the uniform partitions over $[a, b]$, i.e., $x_i = a + \frac{(b-a)(i-1)}{n-1}$ ($i = 1, \dots, n$). Then we have*

$$(3.20) \quad V(f_\Theta; [a, b]) = \lim_{n \rightarrow \infty} \sum_{i=2}^n |f_\Theta(x_i) - f_\Theta(x_{i-1})|.$$

The uniform difference-based TV is the most considered regularization in inverse imaging problems [41, 29, 15, 56, 30], since images are usually defined on uniform meshgrid. From (3.18) & (3.20) we can see that the classical difference-based TV has tight connections with the proposed NeurTV from the infinite perspective, i.e., by taking the limit NeurTV is equivalent to the classical difference-based TV in one-dimensional case:

$$(3.21) \quad V(f_\Theta; [a, b]) = \underbrace{\lim_{n \rightarrow \infty} \sum_{i=2}^n |f_\Theta(x_i) - f_\Theta(x_{i-1})|}_{\text{Difference-based TV}} = \underbrace{\lim_{n \rightarrow \infty} \sum_{i=2}^n |\nabla f_\Theta(x_i)|(x_i - x_{i-1})}_{\text{NeurTV}}.$$

However, in the finite case (i.e., with finite n), NeurTV and difference-based TV are not equivalent, which rationally explains their performance gap for data recovery in the finite condition (see for example Fig. 2). Next, we develop two variants of NeurTV inspired by the variational approximation.

3.5.3. Arbitrary Resolution NeurTV Inspired by Variational Approximation. Inspired by the variational approximation, we develop two variants of NeurTV which further improve its effectiveness. First, we consider the arbitrary resolution NeurTV regularization by using larger number of partitions n in (3.17). Specifically, we show that the truncation error of the numerical integration in (3.17) is related to the interval length $(x_i - x_{i-1})$, which is inversely proportional to the number of partitions n . Hence a larger n is expected to attain relatively lower approximation error of the numerical integration.

Lemma 3.11. *Suppose that $f_\Theta : [a, b] \rightarrow \mathbb{R}$ is continuously differentiable. The truncation error R of numerical integration using uniform partitioned quadrature for approximating the functional TV (i.e., approximating $V(f_\Theta; [a, b])$) satisfies*

$$(3.22) \quad R := |V(f_\Theta; [a, b]) - \sum_{i=2}^n |\nabla f_\Theta(x_i)|(x_i - x_{i-1})| \leq \frac{1}{2} |\nabla^2 f_\Theta(\eta)| (b - a) (x_i - x_{i-1}),$$

where $\eta \in (a, b)$ and ∇^2 denotes the second-order derivative.

Lemma 3.11 shows that the upper bound of the approximation error R is related to the interval length $(x_i - x_{i-1})$, and hence a larger number of partitions n leads to a lower bound of the approximation error. For difference-based TV, we have an analogous lemma.

Lemma 3.12. *Given a differentiable function $f_\Theta : [a, b] \rightarrow \mathbb{R}$, consider the uniform partitions $\mathcal{P}_n := (x_1, \dots, x_n)$ of $[a, b] \subset \mathbb{R}$, i.e., $x_i = a + \frac{(b-a)(i-1)}{n-1}$ ($i = 1, \dots, n$). Then*

$$(3.23) \quad \sum_{\mathcal{P}_n} |f_\Theta(x_i) - f_\Theta(x_{i-1})| \leq \sum_{\mathcal{P}_{2n-1}} |f_\Theta(x_i) - f_\Theta(x_{i-1})| \leq V(f_\Theta; [a, b]).$$

Lemma 3.12 shows that using the difference operators with larger number of partitions (i.e., from n to $2n-1$) leads to lower error for approximating the functional TV, $V(f_\Theta; [a, b])$. Inspired by the variational approximation analysis in Lemmas 3.11-3.12, we can set larger number of partitions n to reduce the approximation error of the functional TV $V(f_\Theta; [a, b])$. We take the image recovery problem as an example. For image recovery, we can sample arbitrary resolution meshgrid beyond the original image resolution to perform the NeurTV regularizations based on the continuous representation $f_\Theta(\cdot)$. More specifically, we consider the following two image recovery models by using the arbitrary resolution NeurTV regularization. First, the derivative-based NeurTV model with arbitrary resolution can be formulated as

$$(3.24) \quad \begin{aligned} \min_{\Theta} \sum_{(i,j) \in \text{meshgrid}} \text{Fidelity}(\mathbf{O}_{(i,j)}, f_\Theta(i, j)) + \lambda \Psi_{\text{NeurTV}}(\Theta), \\ \Psi_{\text{NeurTV}}(\Theta) = \sum_{(i',j') \in \text{denser meshgrid}} |\nabla f_\Theta(i', j')|, \end{aligned}$$

where \mathbf{O} denotes the observed image and λ is a trade-off parameter. In the regularization term $\Psi_{\text{NeurTV}}(\Theta)$, we construct higher-resolution NeurTV beyond the image resolution by using local derivatives of DNN $f_\Theta(\cdot)$ on denser meshgrid. The higher-resolution regularization aims to reduce the approximation error of the numerical integration based on Lemma 3.11. Similarly, we consider the following difference-based NeurTV model with arbitrary resolution:

$$(3.25) \quad \begin{aligned} \min_{\Theta} \sum_{(i,j) \in \text{meshgrid}} \text{Fidelity}(\mathbf{O}_{(i,j)}, f_\Theta(i, j)) + \lambda \Psi_{\text{TV}}(\Theta), \\ \Psi_{\text{NeurTV}}(\Theta) = \sum_{(i',j') \in \text{denser meshgrid}} |f_\Theta(i' + 1, j') - f_\Theta(i', j')| + |f_\Theta(i', j' + 1) - f_\Theta(i', j')|. \end{aligned}$$

In the regularization term $\Psi_{\text{NeurTV}}(\Theta)$, we construct higher-resolution difference-based NeurTV beyond the original image resolution by using the local differences of DNN $f_\Theta(\cdot)$. The numerical experiments in Fig. 14 shall show that a higher-resolution NeurTV regularization (i.e., a larger number of partitions n) inclines to obtain better performances for image recovery. This can be rationally explained by the lower variational approximation error induced by the larger number of partitions n ; see Lemmas 3.12-3.11. In summary, classical TV-based methods [41, 40, 22, 56] utilize discrete representation to construct TV with the original image

Algorithm 3.1 Space-variant NeurTV regularization for image recovery

Input: Observed image $\mathbf{O} \in \mathbb{R}^{n_1 \times n_2}$, trade-off parameter λ , number of partitions n ;

Initialization: Initialize the neural network weights Θ ;

- 1: /* Solving the continuous representation-based image recovery model (3.2) with the space-variant NeurTV regularization $\Psi_{\text{NeurTV}_\theta^\alpha}(\Theta)$ defined in (3.26) */
- 2: **while** not converge **do**
- 3: Compute the function gradient $\nabla f_\Theta(\mathbf{x})$;
- 4: Update scale parameters $\alpha_{\mathbf{x}}$ via (3.27) or (3.28);
- 5: Update directional parameters $a_{\mathbf{x}}, \theta_{\mathbf{x}}$ via (3.29);
- 6: Compute the loss based on model (3.2) with space-variant NeurTV (3.26);
- 7: Update neural network weights Θ by Adam;
- 8: **end while**

Output: The recovered image by querying $f_\Theta(\cdot)$ on meshgrid points;

resolution. Differently, we use the DNN $f_\Theta(\cdot)$ to continuously represent data, which allows us to construct arbitrary resolution NeurTV regularizations to obtain potentially better performances for data recovery.

3.5.4. Space-variant NeurTV Inspired by Variational Approximation. Inspired by the variational approximation analysis, we further develop the space-variant NeurTV regularization, which imposes spatially varying scale and directional parameters to better describe local structures to enhance the flexibility and effectiveness of NeurTV regularizations. Similarly, we consider the two-dimensional case as an example.

Definition 3.13 (Space-variant NeurTV). *Given a two-dimensional differentiable function $f_\Theta : \Omega \rightarrow \mathbb{R}$ where $\Omega \subset \mathbb{R}^2$, a point set $\Gamma \subset \Omega$, and some scale parameters $\alpha_{\mathbf{x}}$ and directional parameters $a_{\mathbf{x}}, \theta_{\mathbf{x}}$ depending on $\mathbf{x} \in \Gamma$, the space-variant NeurTV regularization is defined as*

$$(3.26) \quad \Psi_{\text{NeurTV}_\theta^\alpha}(\Theta) = \sum_{\mathbf{x} \in \Gamma} \alpha_{\mathbf{x}} \left\| \begin{pmatrix} a_{\mathbf{x}} & 0 \\ 0 & 2 - a_{\mathbf{x}} \end{pmatrix} \begin{pmatrix} \cos \theta_{\mathbf{x}} & \sin \theta_{\mathbf{x}} \\ \sin \theta_{\mathbf{x}} & -\cos \theta_{\mathbf{x}} \end{pmatrix} \begin{pmatrix} \nabla_1 f_\Theta(\mathbf{x}) \\ \nabla_2 f_\Theta(\mathbf{x}) \end{pmatrix} \right\|_{\ell_1}.$$

The aim of the space-variant NeurTV is to make distinction between smooth and non-smooth regions by assigning different scale parameters $\alpha_{\mathbf{x}}$ to different elements \mathbf{x} . Meanwhile, the space-variant NeurTV is also capable of distinguishing the local directions of the patterns by assigning different direction parameters $a_{\mathbf{x}}, \theta_{\mathbf{x}}$, where $\theta_{\mathbf{x}}$ and $a_{\mathbf{x}}$ correspond to the direction and the magnitude imposed on the directional derivative with direction $\theta_{\mathbf{x}}$, respectively. According to the directional derivative Lemma 3.2, the regularization $\Psi_{\text{NeurTV}_\theta^\alpha}(\Theta)$ penalizes the derivative along the direction $\theta_{\mathbf{x}}$ with magnitude $a_{\mathbf{x}}$ and penalizes the derivative along the orthogonal direction of $\theta_{\mathbf{x}}$ with magnitude $2 - a_{\mathbf{x}}$. The next step is to design effective strategies to determine the parameters $\alpha_{\mathbf{x}}, a_{\mathbf{x}}, \theta_{\mathbf{x}}$. Inspired by the weighted total variation methods [11, 50], the scale parameter $\alpha_{\mathbf{x}}$ can be simply set as the reciprocal of the local derivative:

$$(3.27) \quad \alpha_{\mathbf{x}} = (|\nabla_1 f_\Theta(\mathbf{x})| + |\nabla_2 f_\Theta(\mathbf{x})| + \epsilon)^{-1},$$

where ϵ is a small constant. The philosophy of this scale parameter selection is to enhance the smoothness over smoother regions while keep the scale parameter smaller in sharper regions

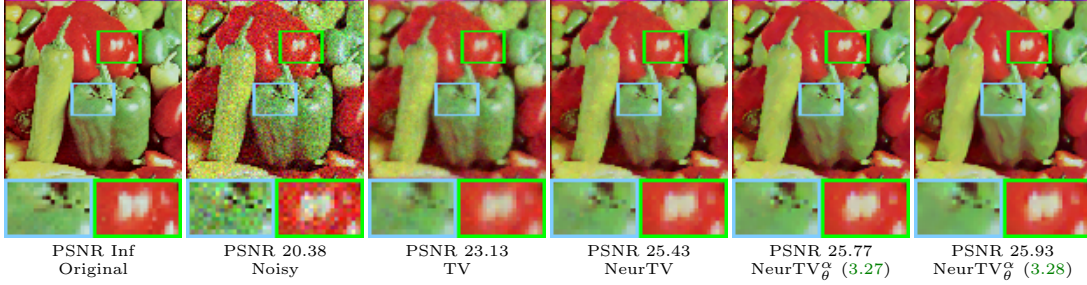


Figure 3. The results of image denoising with Gaussian noise deviation 0.1 using classical TV, the proposed NeurTV regularization, and the proposed space-variant NeurTV regularization (denoted by $\text{NeurTV}_\theta^\alpha$). We consider the first-order derivatives-based scale parameter selection strategy (3.27) or the second-order derivatives-based scale parameter selection strategy (3.28) in the space-variant NeurTV.

with larger derivatives. This can keep the sharpness of the image edges and promote the smoothness of relatively flat regions. In practice, we update the weight $\alpha_{\mathbf{x}}$ based on the learned continuous representation $f_\Theta(\cdot)$ in the last iteration.

Next, we introduce another scale parameter selection strategy specifically designed for our NeurTV inspired by the variational approximation. Specifically, we use the second-order derivative information to determine scale parameters, which was not considered in previous weighted TV-based methods [11, 50]. This selection strategy is inspired by the approximation error analysis of Lemma 3.11, where the variational approximation error is shown to be related to the second-order function derivative. Specifically, we show the following example that if we enlarge the interval of the numerical integration in regions with smaller second-order derivative, then a lower variational approximation error tends to be obtained.

Lemma 3.14. Consider the numerical integration for $V(f, [a, b]) = \int_a^b |\nabla f(x)| dx$ with uniform partitions (x_1, x_2, \dots, x_n) . Assume that $|\nabla f_\Theta(x)|$ is non-decreasing in $[a, b]$ and there exists j such that $\nabla^2 f(t_1) > \nabla^2 f(t_2) \geq 0$ for any $t_1 \in [x_{j-1}, x_j]$ and $t_2 \in [x_j, x_{j+1}]$. Then the truncation error using non-uniform partitions $(x_1, x_2, \dots, x_{j-1}, x_j - \delta, x_{j+1}, \dots, x_n)$ is less than the truncation error using uniform partitions provided that $\delta > 0$ is small enough.

Lemma 3.14 indicates that under mild conditions, a lower approximation error can be obtained by sparing some length δ from intervals with larger second-order derivative to those intervals with smaller second-order derivative. This motivates us to propose the following second-order derivative-based scale parameter selection of the space-variant NeurTV, which assigns larger scale parameters $\alpha_{\mathbf{x}}$ to elements with smaller second-order derivative:

$$(3.28) \quad \alpha_{\mathbf{x}} = (|\nabla_1^2 f_\Theta(\mathbf{x})| + |\nabla_2^2 f_\Theta(\mathbf{x})| + \epsilon)^{-1},$$

where ∇_1^2 and ∇_2^2 respectively denote the second-order derivatives along the first and second dimensions. Similarly, the scale parameter can be updated based on the learned continuous representation $f_\Theta(\cdot)$ in the last iteration.

Next, we further discuss the selection of the directional parameters $a_{\mathbf{x}}, \theta_{\mathbf{x}}$. We propose the following selection schemes for the directional parameters:

$$(3.29) \quad \theta_{\mathbf{x}} = \arctan \frac{\nabla_2 f_\Theta(\mathbf{x})}{\nabla_1 f_\Theta(\mathbf{x})}, \quad a_{\mathbf{x}} = \frac{|(\sin \theta_{\mathbf{x}}, -\cos \theta_{\mathbf{x}}) \nabla f_\Theta(\mathbf{x})|}{|(\cos \theta_{\mathbf{x}}, \sin \theta_{\mathbf{x}}) \nabla f_\Theta(\mathbf{x})|}.$$

Table 1

Summary of the applications considered in experiments and the corresponding NeurTV configuration.

Application	Characteristic	NeurTV configuration	Model	Algorithm
Image denoising	On meshgrid	Space-variant NeurTV (3.26) (with space-variant scales and directions)	(4.1)	Iterative update+Adam (Algorithm 3.1)
Image inpainting	On meshgrid	Space-variant NeurTV (3.26) (with space-variant scales and directions)	(4.2)	Iterative update+Adam (Algorithm 3.1)
Hyperspectral image mixed noise removal	On meshgrid	Spatial-spectral NeurTV (3.11)	(4.3)	Alternating minimization
Point cloud recovery	Beyond meshgrid	Space-variant NeurTV (4.5) (with space-variant scales)	(4.6)	Iterative update+Adam
Spatial transcriptomics reconstruction	Beyond meshgrid	Space-variant NeurTV (3.26) (with space-variant scales and directions)	(4.7)	Iterative update+Adam

In (3.29), the directional parameters $\theta_{\mathbf{x}}$ and $a_{\mathbf{x}}$ are determined by the local derivative information of $f_{\Theta}(\cdot)$, i.e., $\nabla f_{\Theta}(\mathbf{x})$. Specifically, when $\theta_{\mathbf{x}}$ admits (3.29), the directional derivative of $f_{\Theta}(\cdot)$ along the direction $(\cos \theta_{\mathbf{x}}, \sin \theta_{\mathbf{x}})$ attains the maximum intensity for all $\theta_{\mathbf{x}} \in [0, 2\pi)$, and hence we assign a lower weight $a_{\mathbf{x}} < 1$ to this direction to keep the sharpness. In contrast, we assign a larger weight $2 - a_{\mathbf{x}}$ to its orthogonal direction, i.e., $(\sin \theta_{\mathbf{x}}, -\cos \theta_{\mathbf{x}})$, to enhance the smoothness along the orthogonal direction of the gradient. The directional parameters $a_{\mathbf{x}}, \theta_{\mathbf{x}}$ can be updated based on the learned continuous representation $f_{\Theta}(\cdot)$ in the last iteration by using (3.29). We provide a workflow of the space-variant NeurTV regularization-based model for image recovery in Algorithm 3.1.

To numerically validate the effectiveness of our new space-variant NeurTV, we show the results of image recovery using space-variant NeurTV with first-order or second-order derivatives-based scale parameters selection schemes in Fig. 3. We can observe that the space-variant NeurTV obtains better performances than the original NeurTV. Meanwhile, our second-order derivatives-based scale parameters selection scheme (3.28) obtains a better result than the first-order derivatives-based scheme (3.27).

4. Numerical Experiments. In this section, we conduct numerical experiments on different applications with both meshgrid and non-meshgrid data, including image denoising, image inpainting, HSI mixed noise removal, point cloud recovery, and spatial transcriptomics data reconstruction, to show the effectiveness of the proposed NeurTV methods. For easy reference, we first give an intuitive summarization of different applications and the corresponding NeurTV configuration in Table 1.

4.1. Image Denoising (on Meshgrid). First, we conduct the classical image restoration problems on meshgrid. We consider two image restoration tasks, i.e., the image denoising and image inpainting. For the image denoising problem, we consider the following optimization model based on the proposed NeurTV regularization:

$$(4.1) \quad \min_{\Theta} \sum_{(i,j) \in \text{meshgrid}} (\mathbf{O}_{(i,j)} - f_{\Theta}(i, j))^2 + \lambda \Psi_{\text{NeurTV}_{\theta}^{\alpha}}(\Theta),$$

where $\mathbf{O} \in \mathbb{R}^{n_1 \times n_2}$ denotes the observed noisy image and $\Psi_{\text{NeurTV}_{\theta}^{\alpha}}(\Theta)$ denotes the proposed space-variant NeurTV regularization defined in (3.26). λ is a trade-off parameter. The scale parameter α and the directional parameters θ, a in space-variant NeurTV regularization are determined through the schemes presented in (3.28) & (3.29). We use the tensor



Figure 4. The results of image denoising by different methods on “Peppers”, “Boat”, and “House” with Gaussian noise under noise deviation 0.1.

Table 2
The quantitative results by different methods for image denoising.

Noise level	Method	“Peppers”		“Boat”		“House”		“Plane”		“Earth”	
		PSNR	SSIM								
0.1	Noisy	20.38	0.610	20.28	0.642	20.20	0.616	20.12	0.489	20.09	0.562
	TV	23.13	0.768	21.92	0.731	22.43	0.710	23.19	0.660	23.97	0.685
	DIPTV	25.19	0.803	23.33	0.765	23.70	0.753	25.08	0.748	24.48	0.717
	HDTV	25.47	0.822	23.39	0.781	23.83	0.792	25.06	0.785	24.57	0.695
	NeurTV $_{\theta}^{\alpha}$	25.93	0.826	24.67	0.809	24.82	0.823	26.21	0.806	25.12	0.731
0.2	Noisy	14.90	0.385	14.98	0.431	14.71	0.399	14.92	0.309	14.47	0.298
	TV	20.48	0.608	19.69	0.583	20.04	0.559	20.42	0.470	21.01	0.508
	DIPTV	22.02	0.692	20.27	0.631	20.82	0.626	21.94	0.597	22.23	0.544
	HDTV	22.34	0.714	20.37	0.630	20.73	0.636	22.12	0.653	22.54	0.541
	NeurTV $_{\theta}^{\alpha}$	22.46	0.705	21.14	0.664	21.36	0.665	22.60	0.662	22.60	0.546

factorization-based DNN [35] (see Fig. 11 for details) as the function $f_{\Theta} : \mathbb{R}^2 \rightarrow \mathbb{R}$ for continuous representation. The overall algorithm of tackling the denoising model (4.1) is illustrated in Algorithm 3.1. We use the original meshgrid image resolution to define the fidelity term $\sum_{(i,j) \in \text{meshgrid}} (\mathbf{O}_{(i,j)} - f_{\Theta}(i, j))^2$ in (4.1) and use a higher-resolution of meshgrid (three times larger than that of the image) to construct the space-variant NeurTV regularization

$\Psi_{\text{NeurTV}_\theta^\alpha}(\Theta)$, which is expected to obtain better performances as shown in the variational approximation error analysis; see Fig. 14.

The experimental settings of image denoising are as follows. By simple parameter tuning, we fix the trade-off parameter λ as 4×10^{-4} for all datasets. We use three baselines for image denoising, including the classical TV based on ADMM², the TV regularized deep image prior (DIPTV) method [32, 46], and the higher-order directional TV (HDTV) method [40]. We use five color images to test these methods, including “Peppers”, “Boat”, “House”, “Plane”, and “Earth”, which are online available³. The resolution of images are downsampled to fit our computing resources. We add Gaussian noise with the noise standard deviation 0.1 and 0.2 to test different methods. For fair comparison, we denoise the image channel by channel for all methods. The results are quantitatively evaluated by PSNR and SSIM.

The results of image denoising are shown in Table 2 and Fig. 4. We can observe that our method considerably outperforms TV-based methods including the classical TV, DIPTV, and HDTV, which validates the superiority of our NeurTV method. Moreover, the competing TV-based methods are specifically designed for image denoising, while our NeurTV method is more general that can be applied for diverse imaging applications on and beyond meshgrid. Hence, it is rational to say that our method has a wider applicability for different imaging applications.

4.2. Image Inpainting (on Meshgrid). For the image inpainting problem, we assume that the observed image $\mathcal{O} \in \mathbb{R}^{n_1 \times n_2 \times 3}$ (where n_1, n_2 correspond to the spatial dimensions and 3 corresponds to the channel dimension) is incompletely and the index set of observed pixels is denoted by Ω , which is a subset of meshgrid points $\{(i, j, k) | i = 1, 2, \dots, n_1, j = 1, 2, \dots, n_2, k = 1, 2, 3\}$. The goal is to infer the values of the image on the complementary set of Ω (i.e., the missing pixels). We then consider the following optimization model based on the proposed NeurTV regularization for image inpainting:

$$(4.2) \quad \min_{\Theta} \sum_{(i,j,k) \in \Omega} (\mathcal{O}_{(i,j,k)} - f_\Theta(i, j, k))^2 + \lambda \Psi_{\text{NeurTV}_\theta^\alpha}(\Theta),$$

where $\Psi_{\text{NeurTV}_\theta^\alpha}(\Theta)$ denotes the space-variant NeurTV regularization defined in (3.26). The scale parameter α and the directional parameters θ, a in the space-variant NeurTV regularization are determined through (3.28) & (3.29). Here, we impose the space-variant NeurTV on the two spatial dimensions of the color image. For the third dimension (i.e., the channel dimension), we do not impose the NeurTV constraint. We use the tensor factorization-based DNN [35] (see Fig. 11 for details) as the function $f_\Theta : \mathbb{R}^3 \rightarrow \mathbb{R}$ for continuous representation in model (4.2). We use a higher-resolution of meshgrid (three times larger than that of the image) to define the space-variant NeurTV regularization $\Psi_{\text{NeurTV}_\theta^\alpha}(\Theta)$ in model (4.2). The overall algorithm of tackling the model (4.2) is illustrated in algorithm 3.1.

The experimental settings of image inpainting are as follows. We fix the trade-off parameter λ as 3.5×10^{-5} for all datasets. We use three baselines for image inpainting, including the tensor tree decomposition and TV-based method STTC [34], the deep tensor decomposition and TV-based method HLRTF [36], and the tensor correlated TV-based method TCTV

²<https://htmlpreview.github.io/?https://github.com/Yunhui-Gao/total-variation-image-denoising/>

³<https://sipi.usc.edu/database/database.php>

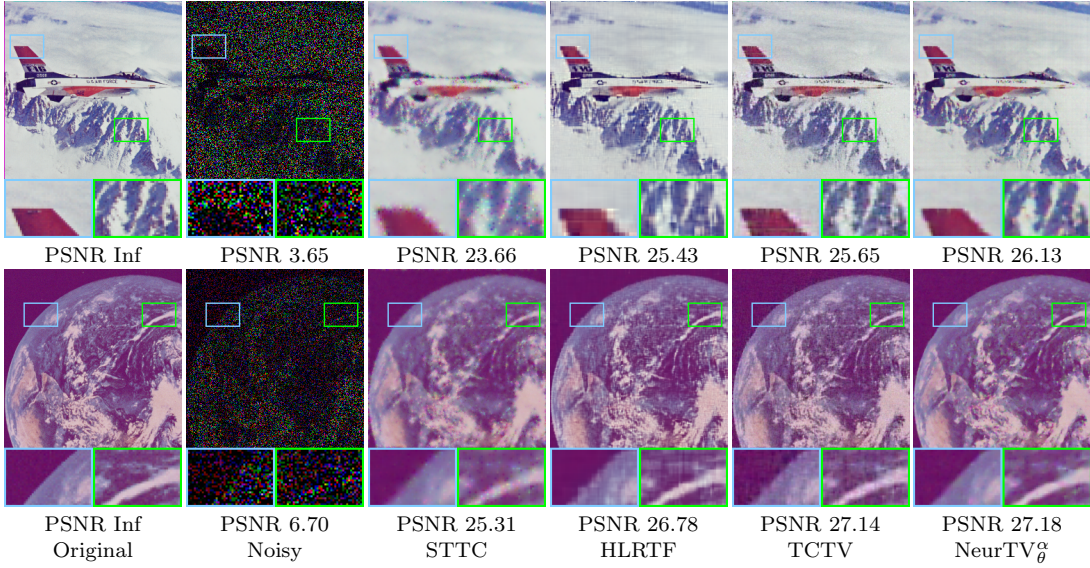


Figure 5. The image inpainting results by different methods on “Plane” and “Earth” with sampling rate 0.2.

Table 3
The quantitative results by different methods for image inpainting.

Sampling rate	Method	“Peppers”		“Boat”		“House”		“Plane”		“Earth”	
		PSNR	SSIM								
0.1	Observed	7.02	0.037	5.63	0.023	4.27	0.014	3.14	0.009	6.18	0.017
	STTC	21.75	0.667	20.43	0.595	20.75	0.630	22.40	0.720	23.71	0.605
	HLRTF	22.48	0.642	21.10	0.575	22.01	0.654	23.31	0.735	24.12	0.604
	TCTV	21.39	0.569	20.70	0.589	21.89	0.662	23.22	0.725	24.64	0.654
	NeurTV $_{\theta}^{\alpha}$	23.74	0.725	21.77	0.650	22.24	0.655	24.10	0.760	24.94	0.661
0.2	Observed	7.53	0.063	6.12	0.05	4.79	0.031	3.65	0.019	6.70	0.032
	STTC	23.45	0.758	21.86	0.693	22.19	0.721	23.66	0.783	25.31	0.708
	HLRTF	24.04	0.725	22.65	0.675	23.35	0.716	25.43	0.816	26.78	0.755
	TCTV	23.94	0.698	22.72	0.698	24.20	0.767	25.65	0.818	27.14	0.766
	NeurTV $_{\theta}^{\alpha}$	25.59	0.793	23.44	0.747	24.11	0.770	26.13	0.840	27.18	0.766

[48]. We use five color images to test these methods, including “Peppers”, “Boat”, “House”, “Plane”, and “Earth”. We consider the sampling rate 0.1 and 0.2 to produce observed incomplete images for testing. The results are quantitatively evaluated by PSNR and SSIM.

The results are shown in Table 3 and Fig. 5. It is seen that our method generally has better performances than other TV-based methods, including STTC, HLRTF, and TCTV. Specifically, our NeurTV quantitatively outperforms other competing methods in most cases, and could also obtain more pleasant visual results for image inpainting as shown in Fig. 5. These results further validate the effectiveness of our NeurTV regularization on meshgrid.

4.3. Hyperspectral Image Mixed Noise Removal (on Meshgrid). Then, we consider the HSI mixed noise removal. The HSI is a type of multi-dimensional data that has multiple spectral bands, allowing the excavation of integral spatial and spectral information. Due to dissatisfied imaging conditions, HSI is often corrupted by random and impulse noise [57, 49], and thus HSI mixed noise removal is a crucial preprocessing step. We assume that the

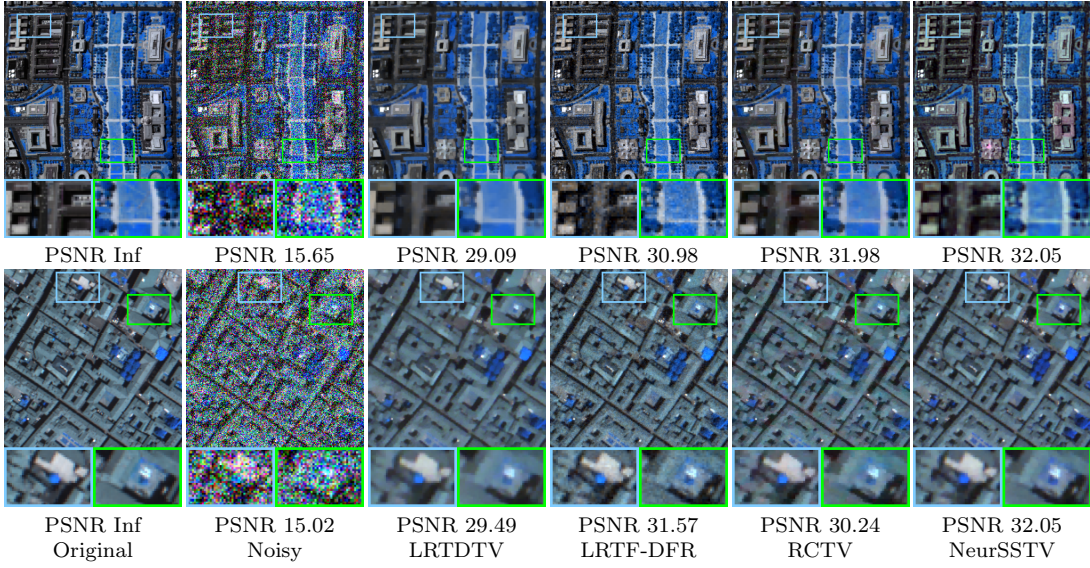


Figure 6. The results of HSI denoising by different methods on “WDC” and “Pavia” with Gaussian noise under noise deviation 0.2.

Table 4
The quantitative results by different methods for HSI mixed noise removal.

Noise level	Method	“WDC”		“Pavia”		“Cloth”		“Cups”		“Fruits”	
		PSNR	SSIM								
Gaussian 0.2	Observed	15.65	0.249	15.02	0.223	19.35	0.285	14.77	0.075	21.89	0.088
	LRTDTV	29.09	0.826	29.49	0.850	30.36	0.776	33.50	0.902	38.77	0.843
	LRTF-DFR	30.98	0.887	31.57	0.910	31.52	0.804	34.30	0.899	38.51	0.804
	RCTV	31.98	0.917	30.24	0.883	29.73	0.739	30.75	0.719	36.54	0.718
	NeurSSTV	32.05	0.917	32.05	0.916	31.64	0.828	36.91	0.960	41.18	0.926
Gaussian 0.2 Impulse 0.1	Observed	12.48	0.153	12.57	0.142	16.60	0.188	12.57	0.049	17.72	0.048
	LRTDTV	27.92	0.790	28.46	0.821	29.36	0.733	32.05	0.856	35.92	0.686
	LRTF-DFR	30.86	0.884	31.12	0.903	31.19	0.795	33.32	0.855	37.86	0.785
	RCTV	30.84	0.897	29.52	0.862	29.13	0.704	30.14	0.697	34.77	0.631
	NeurSSTV	31.63	0.907	31.59	0.912	31.39	0.808	34.87	0.909	39.76	0.844

observed HSI $\mathcal{O} \in \mathbb{R}^{n_1 \times n_2 \times n_3}$ is corrupted by Gaussian and impulse noise. We then consider the following optimization model based on the proposed NeurSSTV regularization (3.11) to capture spatial-spectral local smoothness for HSI mixed noise removal:

$$(4.3) \quad \min_{\Theta, \mathcal{S}} \sum_{(i,j,k) \in \text{meshgrid}} (\mathcal{O}_{(i,j,k)} - f_{\Theta}(i, j, k) - \mathcal{S}_{(i,j,k)})^2 + \lambda \Psi_{\text{NeurSSTV}}(\Theta) + \gamma \|\mathcal{S}\|_{\ell_1},$$

where $\Psi_{\text{NeurSSTV}}(\Theta)$ denotes the proposed NeurSSTV regularization defined in (3.11) and \mathcal{S} denotes the sparse noise to be estimated. We use the tensor factorization-based DNN [35] (see Fig. 11 for details) as the function $f_{\Theta} : \mathbb{R}^3 \rightarrow \mathbb{R}$ for continuous representation in model (4.3). We use a higher-resolution of meshgrid (three times larger than the resolution of HSI) in all three dimensions to define the NeurSSTV regularization. To tackle model (4.2), we consider

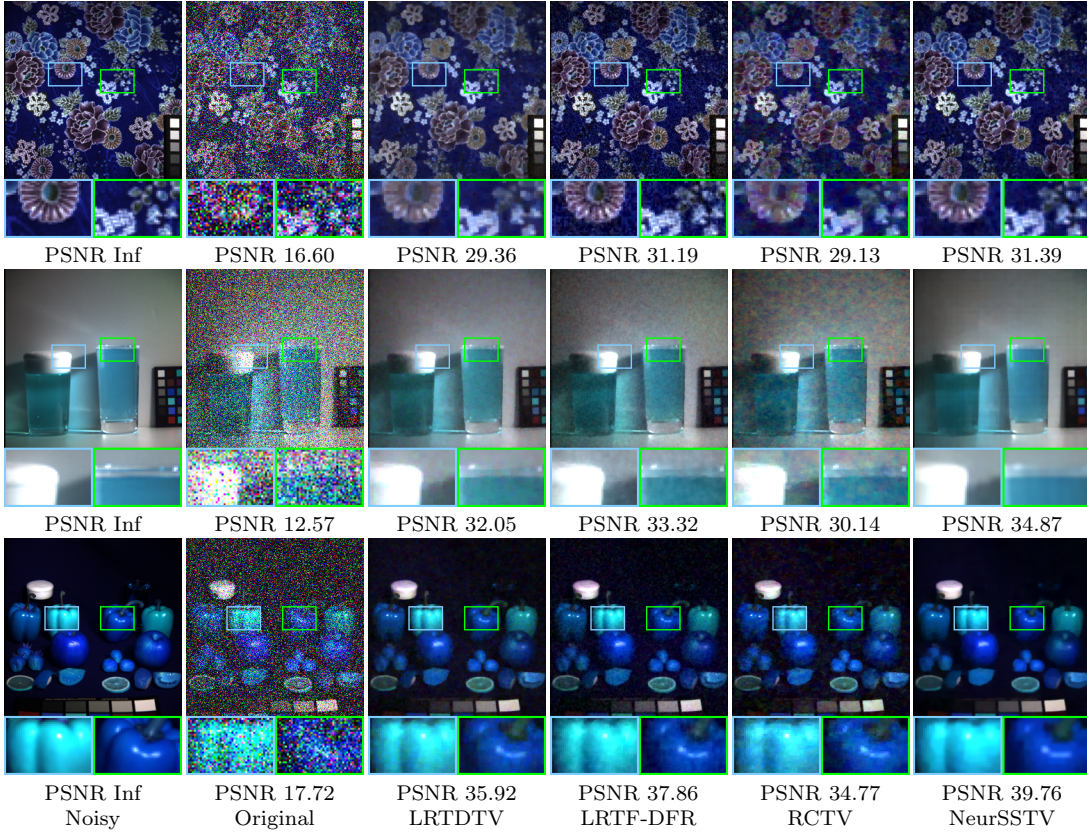


Figure 7. The results of HSI mixed noise removal by different methods on “Cloth”, “Cups”, and “Fruits” with Gaussian noise (noise deviation 0.2) and impulse noise (sampling rate 0.1).

the alternating minimization scheme by tackling the following sub-problems alternately:

$$\begin{aligned}
 (4.4) \quad & \min_{\Theta} \sum_{(i,j,k) \in \text{meshgrid}} (\mathcal{O}_{(i,j,k)} - f_{\Theta}(i, j, k) - \mathcal{S}_{(i,j,k)})^2 + \lambda \Psi_{\text{NeurSSTV}}(\Theta), \\
 & \min_{\mathcal{S}} \sum_{(i,j,k) \in \text{meshgrid}} (\mathcal{O}_{(i,j,k)} - f_{\Theta}(i, j, k) - \mathcal{S}_{(i,j,k)})^2 + \gamma \|\mathcal{S}\|_{\ell_1},
 \end{aligned}$$

where the first problem is tackled by the Adam algorithm [26] and the second one can be tackled by the soft thresholding method.

The experimental settings of HSI mixed noise removal are as follows. We set the trade-off parameters $\lambda = 3 \times 10^{-4}$ and $\gamma = 0.25$ for cases with both Gaussian and impulse noise. For cases with only Gaussian noise, we set $\lambda = 3 \times 10^{-4}$ and $\gamma = 10$. We use three baselines for HSI mixed noise removal, including the tensor decomposition and SSTV-based method LRTDTV [49], the double factor TV-based method LRTF-DFR [57], and the representative coefficient TV-based method RCTV [33]. We use five HSIs to test these methods, including “WDC”, “Pavia”⁴, and three HSIs from the CAVE dataset [51], named “Cloth”, “Cups”, and “Fruits”.

⁴<https://engineering.purdue.edu/~biehl/MultiSpec/hyperspectral.html>

We consider two noisy cases. The first case contains Gaussian noise with noise deviation 0.2. The second case contains mixed Gaussian noise with deviation 0.2 and sparse impulse noise with sampling rate 0.1. The results are quantitatively evaluated by PSNR and SSIM.

The results of HSI mixed noise removal are shown in Table 4 and Figs. 6 & 7. We can observe that our NeurSSTV consistently outperforms other TV-based methods LRTDTV, LRTF-DFR, and RCTV. According to the visual results in Fig. 6, our NeurSSTV could obtain better visual results than other competing methods. Specifically, our NeurSSTV could attenuate the noise well and also preserve the local details of the HSI better. The good performances of our NeurSSTV for HSI mixed noise removal can be rationally explained by the advantage of NeurSSTV, which is able to better capture the higher-order spatial-spectral local correlations of HSI attributed to the continuous nature of neural domain.

4.4. Point Cloud Recovery (Beyond Meshgrid). An intrinsic advantage of NeurTV as compared with classical TV is that NeurTV is suitable for both meshgrid and non-meshgrid data attributed to the continuous representation, while traditional TV is not suitable for non-meshgrid data (e.g., point cloud). To validate this advantage, we consider two types of non-meshgrid data to show the effectiveness of our NeurTV beyond meshgrid, including the point cloud data and the spatial transcriptomics data [47]. First, we consider the point cloud recovery problem, which aims to estimate the color information of all points of the point cloud by giving the color information of some partially sampled points. We assume that the original point cloud with n points is represented by an n -by-5 matrix $\mathbf{O} \in \mathbb{R}^{n \times 5}$, where each point $\mathbf{O}_{(d,:)} (d = 1, 2, \dots, n)$ is an (x, y, z, C, v) format five-dimensional vector, containing coordinate information (i.e., (x, y, z)), channel information (i.e., $C \in \{1, 2, 3\}$), and the corresponding color value v in the channel C at the coordinate (x, y, z) . We split the point cloud \mathbf{O} into training and testing sets. The training dataset contains some pairs of (x, y, z, C) and v information, where the continuous representation $f_\Theta : \mathbb{R}^4 \rightarrow \mathbb{R}$ takes the coordinate and channel vector (x, y, z, C) as the input and is expected to output the corresponding color information v . The testing dataset contains the remaining pairs of (x, y, z, C) and v data to test the trained model.

For the point cloud recovery task, we propose to impose the NeurTV regularization with space-variant scale parameters α in the first three dimensions (x, y, z) and do not impose the constraint in the channel dimension, since the local correlations along channel dimension are not significant. Specifically, suppose that $\mathbf{O}_{\text{train}} \in \mathbb{R}^{n' \times 5}$ denotes the training dataset, a sub-matrix of \mathbf{O} , we then consider the following NeurTV regularization for point cloud data:

$$(4.5) \quad \Psi_{\text{NeurTV}^\alpha}(\Theta) = \sum_{i=1}^{n'} \alpha_i \|(\nabla f_\Theta(\mathbf{O}_{\text{train}_{(i,1:4)}}))_{(1:3)}\|_{\ell_1},$$

where the scale parameter of the i -th sample α_i is determined through the second-order derivatives of the first three dimensions by $\alpha_i = (\sum_{d=1}^3 |\nabla_d^2 f_\Theta(\mathbf{O}_{\text{train}_{(i,1:4)}})| + \epsilon)^{-1}$. Here, we do not consider the space-variant directional parameters since extending the directional NeurTV to three dimensional point cloud is not a trivial task and we leave it to future work. The optimization model of training the continuous representation $f_\Theta(\cdot)$ for point cloud recovery is

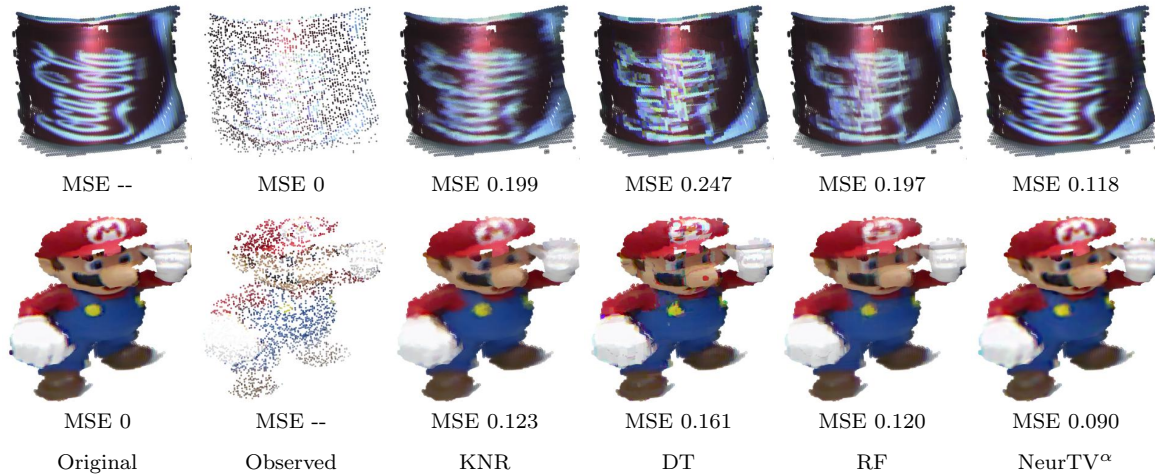


Figure 8. The results of point cloud recovery by different methods on “Cola” and “Mario” with sampling rate 0.2.

Table 5
The quantitative results by different methods for point cloud recovery.

Sampling rate	Method	“Cola”		“Mario”		“Duck”		“Squirrel”		“Rabbit”	
		MSE	R-Square								
0.1	KNR	0.264	0.787	0.162	0.912	0.108	0.891	0.153	0.820	0.135	0.841
	DT	0.332	0.692	0.211	0.856	0.133	0.841	0.164	0.802	0.170	0.766
	RF	0.257	0.799	0.152	0.922	0.098	0.910	0.140	0.851	0.130	0.853
	NeurTV $^\alpha$	0.191	0.889	0.126	0.947	0.087	0.929	0.126	0.878	0.108	0.899
0.2	KNR	0.199	0.879	0.123	0.949	0.082	0.937	0.114	0.901	0.104	0.906
	DT	0.247	0.821	0.161	0.915	0.095	0.917	0.133	0.868	0.126	0.867
	RF	0.197	0.882	0.120	0.952	0.071	0.954	0.105	0.916	0.099	0.915
	NeurTV $^\alpha$	0.118	0.957	0.090	0.973	0.067	0.958	0.085	0.945	0.079	0.945

formulated as:

$$(4.6) \quad \min_{\Theta} \sum_{i=1}^{n'} (\mathbf{O}_{\text{train}_{(i,5)}} - f_{\Theta}(\mathbf{O}_{\text{train}_{(i,1:4)}}))^2 + \lambda \Psi_{\text{NeurTV}^{\alpha}}(\Theta).$$

We use the tensor factorization-based DNN [35] (see Fig. 11 for details) as the function $f_{\Theta} : \mathbb{R}^4 \rightarrow \mathbb{R}$ for continuous representation in model (4.6). The algorithm of tackling the point cloud recovery model (4.6) is similar to Algorithm 3.1 by using iterative updates of the scale parameters α_i and the DNN weights Θ .

The experimental settings of point cloud recovery are as follows. We set the trade-off parameter $\lambda = 1 \times 10^{-4}$, and then use three regression methods as baselines for point cloud recovery, including the K-neighbors regressor (KNR), the decision tree (DT) regressor, and the random forest (RF). Five point cloud datasets are used to test these methods, including “Cola”, “Mario”, “Duck”, “Squirrel”, and “Rabbit”, which are online available⁵. We consider the sampling rate of training dataset as 0.1 and 0.2 to test different methods. The results are quantitatively evaluated by normalized root MSE and R-Square.

⁵<http://www.vision.deis.unibo.it/research/80-shot>

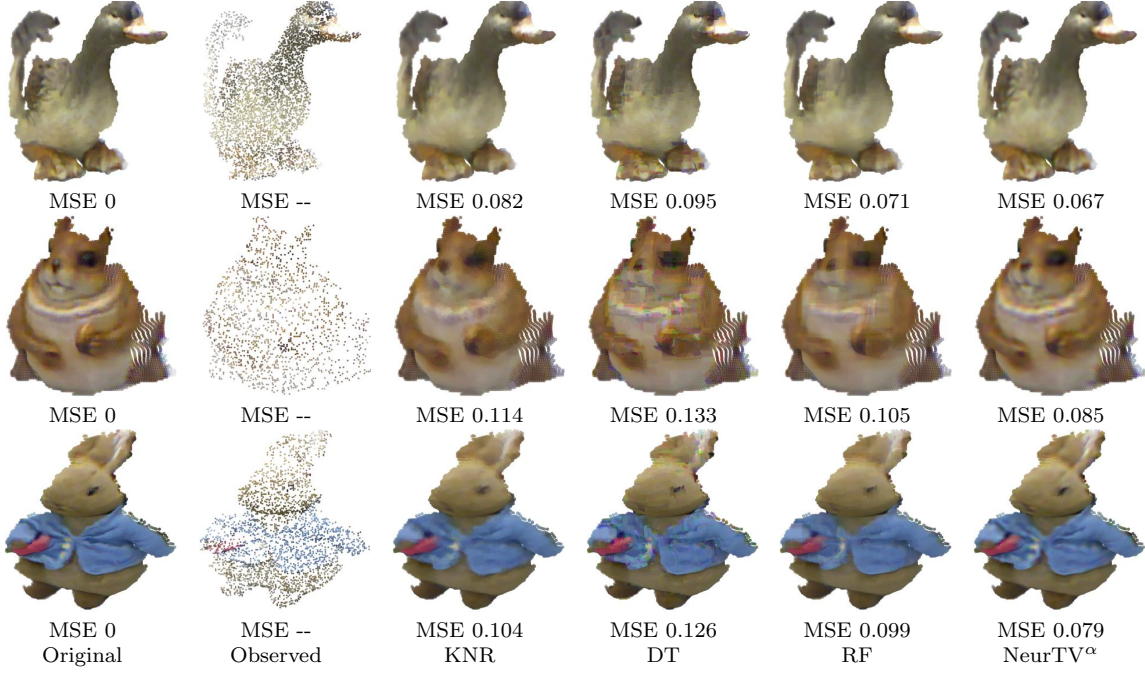


Figure 9. The results of point cloud recovery by different methods on “Duck”, “Squirrel”, and “Rabbit” with sampling rate 0.2.

The results of point cloud recovery are shown in Table 5 and Figs. 8 & 9. We can observe that our NeurTV method quantitatively outperforms other competing methods for point cloud recovery, which validates the effectiveness of NeurTV beyond meshgrid. From the visual results in Fig. 8, we can observe that our NeurTV could better recover the local structures and color information of the point clouds, which further verify its capability to characterize the structures of point cloud data beyond meshgrid.

4.5. Spatial Transcriptomics Reconstruction (Beyond Meshgrid). Spatial transcriptomics data [47, 44] is a novel, non-meshgrid, and important biological data that reveals informative gene expressions over a spatial area of tissues. The spatial transcriptomics data has been well recognized as a next-generation approach for many biological analysis tasks [37]. A distinct feature of spatial transcriptomics data is that it is not arranged as meshgrid data but rather placed at non-meshgrid points in the spatial area due to the sequencing technology and the non-cubic shape of tissues, which poses challenges for classical methods like TV for characterizing it. As compared, our NeurTV benefits from the continuous representation and is suitable for spatial transcriptomics data. Specifically, we consider the spatial transcriptomics reconstruction problem [44], which aims to reconstruct the whole spatial transcriptomics from the partially sampled observation.

We assume that the original three-dimensional transcriptomics data with n samples is represented by an n -by-4 matrix $\mathbf{O} \in \mathbb{R}^{n \times 4}$. Each vector sample $\mathbf{O}_{(d,:)} (d = 1, 2, \dots, n)$ is an (x, y, g, v) format four-dimensional vector, where (x, y) denotes the spatial coordinate, g corresponds to a gene type, and v is the gene expression of the gene g at the spot with coordinate (x, y) . We split the data \mathbf{O} into training and testing sets. The training dataset

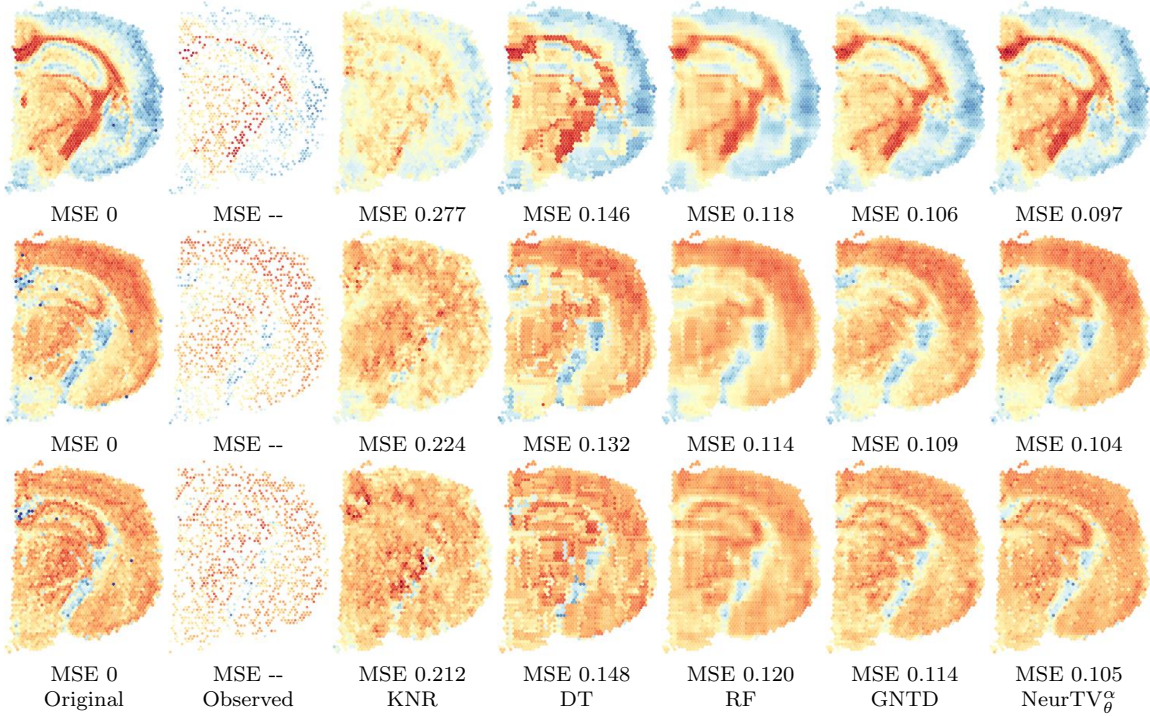


Figure 10. The results of spatial transcriptomics data reconstruction by different competing methods. The three rows respectively list the results of all comparison methods on genes “mbp”, “snap25”, and “atp1b1” of the mouse brain dataset with sampling rate 0.4.

Table 6

The quantitative results by different methods for spatial transcriptomics reconstruction on different genes of the mouse brain dataset.

Sampling rate	Method	“mbp”		“snap25”		“atp1b1”		“plp1”		“rtn1”	
		MSE	R-Square								
0.3	KNR	0.299	0.352	0.232	0.125	0.215	0.030	0.417	0.242	0.183	0.396
	DT	0.177	0.737	0.148	0.619	0.171	0.331	0.275	0.639	0.161	0.553
	RF	0.138	0.837	0.118	0.737	0.127	0.539	0.234	0.728	0.130	0.669
	GNTD	0.125	0.873	0.117	0.744	0.121	0.584	0.216	0.768	0.125	0.694
	NeurTV $_{\theta}^{\alpha}$	0.113	0.890	0.113	0.768	0.117	0.635	0.197	0.809	0.120	0.735
0.4	KNR	0.277	0.445	0.224	0.147	0.212	0.034	0.381	0.382	0.172	0.452
	DT	0.146	0.820	0.132	0.686	0.148	0.432	0.242	0.710	0.140	0.642
	RF	0.118	0.880	0.114	0.754	0.120	0.584	0.204	0.791	0.117	0.724
	GNTD	0.106	0.903	0.109	0.774	0.114	0.621	0.186	0.826	0.117	0.726
	NeurTV $_{\theta}^{\alpha}$	0.097	0.916	0.104	0.796	0.105	0.680	0.164	0.860	0.107	0.768

contains some pairs of (x, y, g) and v information, where the continuous representation $f_{\Theta} : \mathbb{R}^3 \rightarrow \mathbb{R}$ takes the coordinate and gene vector (x, y, g) as input and is expected to output the corresponding gene expression value v . The testing dataset contains the remaining pairs of (x, y, g) and v data to test the trained model. Suppose that $\mathbf{O}_{\text{train}} \in \mathbb{R}^{n' \times 4}$ denotes the training dataset, which is a sub-matrix of \mathbf{O} . We then consider the following optimization model for training the continuous representation $f_{\Theta}(\cdot)$ based on the space-variant NeurTV

regularization:

$$(4.7) \quad \min_{\Theta} \sum_{i=1}^{n'} (\mathbf{O}_{\text{train}_{(i,4)}} - f_{\Theta}(\mathbf{O}_{\text{train}_{(i,1:3)}}))^2 + \lambda \Psi_{\text{NeurTV}_{\theta}^{\alpha}}(\Theta),$$

where $\Psi_{\text{NeurTV}_{\theta}^{\alpha}}(\Theta)$ denotes the proposed space-variant NeurTV regularization defined in (3.26). We impose the NeurTV constraint in the spatial dimensions (x, y) and do not impose the constraint in the gene dimension g since the local correlations in the gene dimension are not significant. We use the tensor factorization-based DNN [35] (see Fig. 11 for details) as the function $f_{\Theta} : \mathbb{R}^3 \rightarrow \mathbb{R}$ for continuous representation in model (4.7). The algorithm of tackling the model (4.7) is similar to Algorithm 3.1 by using iterative updates of the scale and directional parameters α, θ, a and the DNN weights Θ .

The experimental settings of spatial transcriptomics reconstruction are as follows. We set the trade-off parameter λ as 2.5×10^{-4} , and use four baselines, including the three regression methods KNR, DT, RF, and a graph tensor decomposition-based method GNTD [44]. We use the spatial transcriptomics data of a mouse brain dataset from the 10x Genomics⁶ to test these methods for spatial transcriptomics reconstruction, and extract five gene types in the dataset for testing, including the genes “mbp”, “snap25”, “atp1b1”, “plp1”, and “rtn1”. We consider the sampling rate of training dataset as 0.3 and 0.4 and use the trained models to reconstruct the data (i.e., predicting the gene expression at unobserved points). The results are quantitatively evaluated by normalized root MSE and R-Square.

The results of spatial transcriptomics reconstruction are shown in Table 6 and Fig. 10. It can be observed that our NeurTV quantitatively outperforms the other methods. Especially, our method outperforms GNTD [44], which is a state-of-the-art method for spatial transcriptomics reconstruction. The visual results in Fig. 10 show that our NeurTV can better identify local structures of the spatial transcriptomics and recover the spatial gene expressions more accurately than other comparison methods. These results substantiate the effectiveness of our method for the spatial transcriptomics reconstruction task beyond meshgrid.

4.6. Influence of Different Architectures. Our NeurTV regularization is a basic building block that can be combined with different DNN architectures to capture local correlations of data. Here, we take three DNNs as examples, i.e., the sine function-based [43], the positional encoding (PE)-based [45], and the tensor factorization (TF)-based [35] DNNs, which have been shown to be effective for continuous representation of data. A general illustration of these DNNs is shown in Fig. 11. The formulations of these DNN are listed below.

$$(4.8) \quad \begin{aligned} & (\text{Sine function-based DNN}) f_{\Theta}(\mathbf{x}) = \mathbf{W}_K \sin(\mathbf{W}_{K-1} \cdots \sin(\mathbf{W}_1 \mathbf{x})), \\ & (\text{PE-based DNN}) f_{\Theta}(\mathbf{x}) = \mathbf{W}_K \text{ReLU}(\mathbf{W}_{K-1} \cdots \text{ReLU}(\mathbf{W}_1 \text{PE}(\mathbf{x}))), \\ & (\text{Tensor factorization-based DNN}) f_{\Theta}(\mathbf{x}) = \mathcal{C} \times_1 f_{\Theta_1}(\mathbf{x}_{(1)}) \times_2 f_{\Theta_2}(\mathbf{x}_{(2)}) \times_3 f_{\Theta_3}(\mathbf{x}_{(3)}), \end{aligned}$$

where $\{\mathbf{W}_k\}_{k=1}^K$ denote the weight matrices of the fully connected (FC) layers, $\text{PE}(\mathbf{x}) := [a_1 \cos(2\pi \mathbf{b}_1^T \mathbf{x}), a_1 \sin(2\pi \mathbf{b}_1^T \mathbf{x}), \dots, a_m \cos(2\pi \mathbf{b}_m^T \mathbf{x}), a_m \sin(2\pi \mathbf{b}_m^T \mathbf{x})]^T$ denotes the PE layer, \mathcal{C} denotes a core tensor, and $\{f_{\Theta_d}\}_{d=1}^3$ denote three FC networks. More concrete structures of

⁶<https://www.10xgenomics.com/datasets>

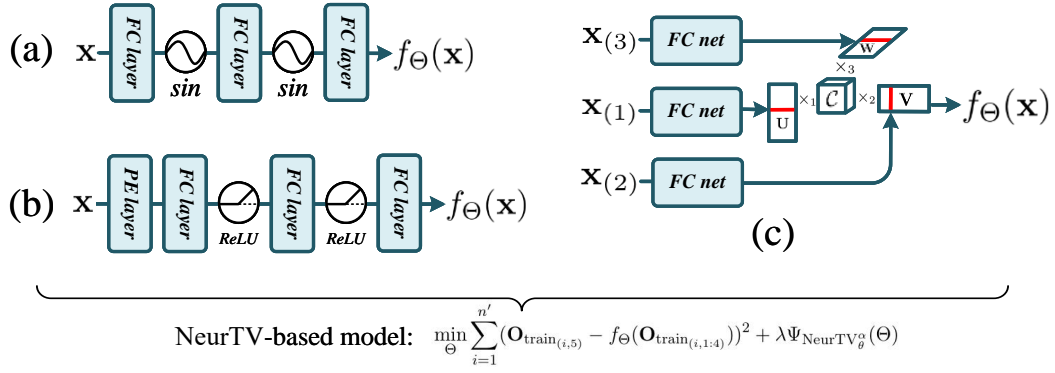


Figure 11. Our NeurTV regularization is a basic building block that can be combined with different DNNs $f_\Theta(\cdot)$. For instance we consider (a) the sine function-based DNN [43], (b) the positional encoding (PE)-based DNN [45], and (c) the tensor factorization (TF)-based DNN [35] to show the effectiveness and compatibility of our NeurTV method.

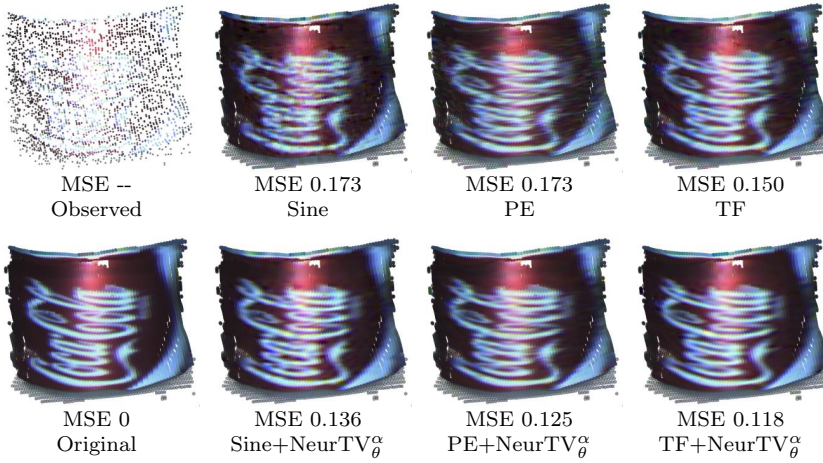
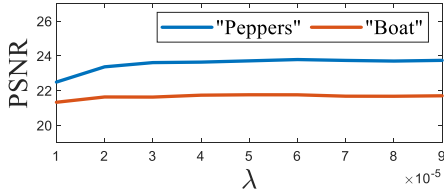


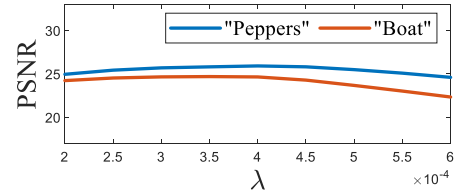
Figure 12. The results of point cloud recovery using different DNNs (sine function-based [43], PE-based [45], and TF-based [35] DNNs) with and without the proposed space-variant NeurTV regularization (3.26).

these DNNs can be found in relevant references [43, 45, 35]. Our NeurTV regularization can be easily combined with these DNNs by using the NeurTV-based data recovery model, e.g., model (4.6). Here, we take the point cloud recovery as an example by using the proposed space-variant NeurTV model (4.6) with different DNNs. The results are shown in Fig. 12. We can observe that the space-variant NeurTV regularization consistently improves the performances of point cloud recovery by using different DNN architectures, demonstrating its effectiveness and good compatibility.

4.7. Influence of Hyperparameters. In this subsection, we test the influence of hyperparameters in our method. For regularization-based methods, the setting of the trade-off hyperparameter λ is crucial for attaining good performance. Here, we evaluate the sensitivity of our NeurTV models (e.g., models (4.1) & (4.2)) w.r.t. the value of the trade-off hyperparameter λ . In Fig. 13, we plot the PSNR value of the image recovery result by using the



(a) Image inpainting



(b) Image denoising

Figure 13. The PSNR w.r.t. the value of the trade-off parameter λ by using our space-variant NeurTV for (a) image inpainting with sampling rate 0.1 and (b) image denoising with Gaussian noise deviation 0.1.

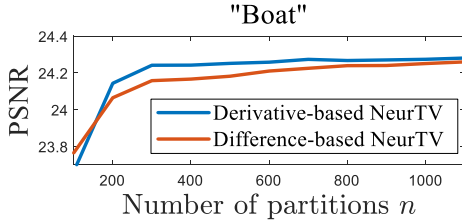
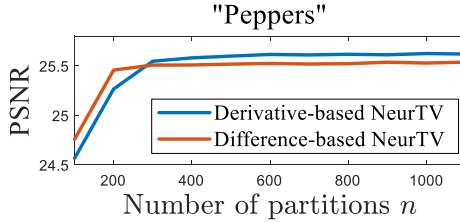


Figure 14. The PSNR w.r.t. the number of partitions n for image denoising with noise deviation 0.1 by using the derivative-based NeurTV model (3.24) and the difference-based NeurTV model (3.25).

space-variant NeurTV with different values of the trade-off hyperparameter λ . We can observe that our method could attain satisfactory PSNR values for a wide range of λ , which validates the robustness of our method w.r.t. the trade-off hyperparameter.

Meanwhile, the number of partitions n is another important hyperparameter in our NeurTV-based models, e.g., models (3.24) & (3.25). Here, we change the number of partitions and test our NeurTV-based models (3.24) & (3.25) for image denoising. The results are shown in Fig. 14. It is clear that larger n inclines to obtain better performances for both derivative-based and difference-based NeurTV models, which coincides with the variational approximation analysis in Lemmas 3.11-3.12. Moreover, the NeurTV models obtain satisfactory PSNR values for a wide range of n , validating its robustness w.r.t. this hyperparameter.

5. Conclusion. In this work, we have proposed the NeurTV regularization to capture local correlations of data based on continuous representation. As compared with classical discrete meshgrid-based TV, our NeurTV enjoys two advantages. First, NeurTV is suitable for both meshgrid and non-meshgrid data and hence has wider applicability than classical TV. Second, by virtue of the continuous and differentiable nature of DNN, our NeurTV can be readily extended to capture local correlations of data for any direction and any order of derivatives more accurately than classical TV. We have reinterpreted NeurTV from the variational approximation perspective, which allowed us to draw its connections with classical TV and motivated us to develop variants such as arbitrary resolution and space-variant NeurTV regularizations. Numerical experiments on different inverse imaging problems with meshgrid (e.g., color images and HSIs) and non-meshgrid (e.g., point clouds and spatial transcriptomics) data validated the effectiveness and superiority of our NeurTV regularization methods.

Appendix A. Proof of Lemmas.

Lemma 3.9. For a continuously differentiable function $f_\Theta : [a, b] \rightarrow \mathbb{R}$, its functional TV

(3.12) is equal to

(A.1)

$$V(f_\Theta; [a, b]) = \int_a^b |\nabla f_\Theta(x)| dx = \sup_{\mathcal{P}} \left\{ \sum_{i=2}^n |f_\Theta(x_i) - f_\Theta(x_{i-1})| : n \in \mathbb{N}, \mathcal{P} = (x_1, \dots, x_n) \right\},$$

where \mathcal{P} are some partitions over $[a, b]$ with $x_1 = a$ and $x_n = b$.

Proof. The first equality follows from Lemma 3.7 and we show the second equality as follows. For any partitions $\mathcal{P} = (x_1, \dots, x_n)$ we have

$$\begin{aligned} (A.2) \quad \sum_{i=2}^n |f_\Theta(x_i) - f_\Theta(x_{i-1})| &= \sum_{i=2}^n \left| \int_{x_{i-1}}^{x_i} \nabla f_\Theta(x) dx \right| \\ &\leq \sum_{i=2}^n \int_{x_{i-1}}^{x_i} |\nabla f_\Theta(x)| dx = \int_a^b |\nabla f_\Theta(x)| dx. \end{aligned}$$

Hence we have $\sup_{\mathcal{P}} \left\{ \sum_{i=2}^n |f_\Theta(x_i) - f_\Theta(x_{i-1})| \right\} \leq \int_a^b |\nabla f_\Theta(x)| dx$.

On the other hand, using mid-value theorem we have

$$(A.3) \quad \sum_{i=2}^n |f_\Theta(x_i) - f_\Theta(x_{i-1})| = \sum_{i=2}^n |\nabla f_\Theta(\xi_i)|(x_i - x_{i-1}),$$

where $\xi_i \in (x_{i-1}, x_i)$. Let $\eta_i := \inf_{x \in (x_{i-1}, x_i)} |\nabla f_\Theta(x)|$, then we have

$$(A.4) \quad \sum_{i=2}^n |f_\Theta(x_i) - f_\Theta(x_{i-1})| = \sum_{i=2}^n |\nabla f_\Theta(\xi_i)|(x_i - x_{i-1}) \geq \sum_{i=2}^n \eta_i(x_i - x_{i-1}).$$

Taking supremum over all partitions \mathcal{P} on both sides, we have

$$(A.5) \quad \sup_{\mathcal{P}} \left\{ \sum_{i=2}^n |f_\Theta(x_i) - f_\Theta(x_{i-1})| \right\} \geq \sup_{\mathcal{P}} \left\{ \sum_{i=2}^n \eta_i(x_i - x_{i-1}) \right\} = \int_a^b |\nabla f_\Theta(x)| dx,$$

where the last equality follows from the definition of integral. ■

Lemma 3.10. For a differentiable function $f_\Theta : [a, b] \rightarrow \mathbb{R}$, we consider the uniform partitions over $[a, b]$, i.e., $x_i = a + \frac{(b-a)(i-1)}{n-1}$ ($i = 1, \dots, n$). Then we have

$$(A.6) \quad V(f_\Theta; [a, b]) = \lim_{n \rightarrow \infty} \sum_{i=2}^n |f_\Theta(x_i) - f_\Theta(x_{i-1})|.$$

Proof. Given any partitions $\mathcal{P} = (x_1, \dots, x_n)$, denote $V_{\mathcal{P}}(f_\Theta; [a, b]) := \sum_{i=2}^n |f_\Theta(x_i) - f_\Theta(x_{i-1})|$. For any $\epsilon > 0$, according to Lemma 3.9 there exist some partitions $\mathcal{P}' = (x'_1, x'_2, \dots, x'_m)$ such that

$$(A.7) \quad V(f_\Theta; [a, b]) - \frac{\epsilon}{2} < V_{\mathcal{P}'}(f_\Theta; [a, b]) \leq V(f_\Theta; [a, b]).$$

Since $f_\Theta(\cdot)$ is continuous in the interval $[a, b]$, there exists $\delta > 0$ such that $|f_\Theta(x) - f_\Theta(y)| < \epsilon/(4m)$ for any $|x - y| < \delta$. Consider an uniform partition $\mathcal{P}'' = (x_1'', \dots, x_n'')$ such that $\|\mathcal{P}''\| := \max_{i=2,3,\dots,n} |x_i'' - x_{i-1}''| < \delta$. Let $\mathcal{P} = \mathcal{P}' \cup \mathcal{P}''$. Then we have $\|\mathcal{P}\| < \delta$ and

$$(A.8) \quad V_{\mathcal{P}'}(f_\Theta; [a, b]) < V_{\mathcal{P}}(f_\Theta; [a, b]), \quad V_{\mathcal{P}''}(f_\Theta; [a, b]) < V_{\mathcal{P}}(f_\Theta; [a, b]).$$

Note that adding every point x'_i ($i = 1, \dots, m$) in \mathcal{P}' to the partitions \mathcal{P}'' leads to an increase of function variation at most $2\epsilon/4m$ since $\|\mathcal{P}' \cup \mathcal{P}''\| = \|\mathcal{P}\| < \delta$. Hence the total increase of function variation of $V_{\mathcal{P}}(f_\Theta; [a, b])$ against $V_{\mathcal{P}''}(f_\Theta; [a, b])$ admits

$$(A.9) \quad V_{\mathcal{P}}(f_\Theta; [a, b]) - \frac{\epsilon}{2} \leq V_{\mathcal{P}''}(f_\Theta; [a, b]).$$

Hence we have

$$(A.10) \quad \begin{aligned} V(f_\Theta; [a, b]) - \epsilon &\leq V_{\mathcal{P}'}(f_\Theta; [a, b]) - \frac{\epsilon}{2} \leq V_{\mathcal{P}}(f_\Theta; [a, b]) - \frac{\epsilon}{2} \\ &\leq V_{\mathcal{P}''}(f_\Theta; [a, b]) \leq V(f_\Theta; [a, b]). \end{aligned}$$

Let $\epsilon \rightarrow 0$ we have $V(f_\Theta; [a, b]) = V_{\mathcal{P}''}(f_\Theta; [a, b])$ with $\delta \rightarrow 0$, i.e., with $n \rightarrow \infty$. Hence $V(f_\Theta; [a, b]) = \lim_{n \rightarrow \infty} V_{\mathcal{P}''}(f_\Theta; [a, b])$. \blacksquare

Lemma 3.11. *Suppose that $f_\Theta : [a, b] \rightarrow \mathbb{R}$ is continuously differentiable. The truncation error R of numerical integration using uniform partitioned quadrature for approximating the functional TV (i.e., approximating $V(f_\Theta; [a, b])$) satisfies*

$$(A.11) \quad R := |V(f_\Theta; [a, b]) - \sum_{i=2}^n |\nabla f_\Theta(x_i)|(x_i - x_{i-1})| \leq \frac{1}{2} |\nabla^2 f_\Theta(\eta)|(b - a)(x_i - x_{i-1}),$$

where $\eta \in (a, b)$ and ∇^2 denotes the second-order derivative.

Proof. For any $i = 2, 3, \dots, n$, we have

$$(A.12) \quad \begin{aligned} \int_{x_{i-1}}^{x_i} |\nabla f_\Theta(x)| dx - |\nabla f_\Theta(x_i)|(x_i - x_{i-1}) &= \int_{x_{i-1}}^{x_i} (|\nabla f_\Theta(x)| - |\nabla f_\Theta(x_i)|) dx \\ &\leq \int_{x_{i-1}}^{x_i} |\nabla f_\Theta(x) - \nabla f_\Theta(x_i)| dx = \int_{x_{i-1}}^{x_i} |\nabla^2 f_\Theta(\xi_i)(x_i - x)| dx \\ &= \int_{x_{i-1}}^{x_i} |\nabla^2 f_\Theta(\xi_i)|(x_i - x) dx = |\nabla^2 f_\Theta(\eta_i)| \int_{x_{i-1}}^{x_i} (x_i - x) dx, \end{aligned}$$

where $\xi_i \in [x_{i-1}, x]$ is a function of x and $\eta_i \in [x_{i-1}, x_i]$. The last equality follows from the mean value theorem of integral provided that $(x_i - x) \geq 0$ for $x \in [x_{i-1}, x_i]$ and $|\nabla^2 f_\Theta(\xi_i)|$ is a continuous function w.r.t. x . Summing the error from $i = 2, 3, \dots, n$ we have

$$(A.13) \quad \begin{aligned} R &:= \left| \sum_{i=2}^n \left(\int_{x_{i-1}}^{x_i} |\nabla f_\Theta(x)| dx - |\nabla f_\Theta(x_i)|(x_i - x_{i-1}) \right) \right| \leq \sum_{i=2}^n |\nabla^2 f_\Theta(\eta_i)| \int_{x_{i-1}}^{x_i} (x_i - x) dx \\ &= \frac{1}{2} (n-1) |\nabla^2 f_\Theta(\eta)| (x_i - x_{i-1})^2, \end{aligned}$$

where the last equality follows from the intermediate value theorem provided that $|\nabla^2 f_\Theta(x)|$ is continuous w.r.t. x in $[a, b]$ and $\eta \in (a, b)$. Further calculate yields

$$(A.14) \quad R \leq \frac{1}{2}(n-1)|\nabla^2 f_\Theta(\eta)|(x_i - x_{i-1})^2 = \frac{1}{2}|\nabla^2 f_\Theta(\eta)|(b-a)(x_i - x_{i-1}),$$

which completes the proof. \blacksquare

Lemma 3.12. *Given a differentiable function $f_\Theta : [a, b] \rightarrow \mathbb{R}$. Consider the uniform partitions $\mathcal{P}_n := (x_1, \dots, x_n)$ of $[a, b] \subset \mathbb{R}$, i.e., $x_i = a + \frac{(b-a)(i-1)}{n-1}$ ($i = 1, \dots, n$). Then*

$$(A.15) \quad \sum_{\mathcal{P}_n} |f_\Theta(x_i) - f_\Theta(x_{i-1})| \leq \sum_{\mathcal{P}_{2n}} |f_\Theta(x_i) - f_\Theta(x_{i-1})| \leq V(f_\Theta; [a, b]).$$

Proof. The first inequality follows from the triangle inequality, i.e.,

$$(A.16) \quad |f_\Theta(x_i) - f_\Theta(x_{i-1})| \leq |f_\Theta((x_{i-1} + x_i)/2) - f_\Theta(x_{i-1})| + |f_\Theta(x_i) - f_\Theta((x_{i-1} + x_i)/2)|,$$

and the second inequality follows from Lemma 3.9. \blacksquare

Lemma 3.14. *Consider the numerical integration for $V(f, [a, b]) = \int_a^b |\nabla f(x)| dx$ with uniform partitions (x_1, x_2, \dots, x_n) . Assume that $|\nabla f_\Theta(x)|$ is non-decreasing in $[a, b]$ and there exists j such that $\nabla^2 f(t_1) > \nabla^2 f(t_2) \geq 0$ for any $t_1 \in [x_{j-1}, x_j]$ and $t_2 \in [x_j, x_{j+1}]$. Then the truncation error using non-uniform partitions $(x_1, x_2, \dots, x_{j-1}, x_j - \delta, x_{j+1}, \dots, x_n)$ is less than the truncation error using uniform partitions provided that $\delta > 0$ is small enough.*

Proof. Since $|\nabla f_\Theta(x)|$ is non-decreasing we have $|\nabla f_\Theta(x)| - |\nabla f_\Theta(x_i)| \leq 0$ for $x \in [x_{i-1}, x_i]$, and hence $\int_{x_{i-1}}^{x_i} (|\nabla f_\Theta(x)| - |\nabla f_\Theta(x_i)|) dx \leq 0$ for $i = 2, \dots, n$. Denote R_1 the truncation error of numerical integration using uniform partitions (x_1, x_2, \dots, x_n) . We have

$$(A.17) \quad R_1 = \left| \sum_{i=2}^n \int_{x_{i-1}}^{x_i} (|\nabla f_\Theta(x)| - |\nabla f_\Theta(x_i)|) dx \right| = \sum_{i=2}^n \int_{x_{i-1}}^{x_i} (|\nabla f_\Theta(x_i)| - |\nabla f_\Theta(x)|) dx.$$

Let $\delta \in (0, x_j - x_{j-1})$. Denote R_2 the truncation error of numerical integration using non-uniform partitions $(x_1, \dots, x_{j-1}, x_j - \delta, x_{j+1}, \dots, x_n)$ and note that $|\nabla f_\Theta(x)|$ is non-decreasing in $[a, b]$. We have

$$(A.18) \quad \begin{aligned} R_2 &= \sum_{i \neq j, j+1} \int_{x_{i-1}}^{x_i} (|\nabla f_\Theta(x_i)| - |\nabla f_\Theta(x)|) dx + \int_{x_{j-1}}^{x_j - \delta} (|\nabla f_\Theta(x_j - \delta)| - |\nabla f_\Theta(x)|) dx \\ &\quad + \int_{x_j - \delta}^{x_j} (|\nabla f_\Theta(x_{j+1})| - |\nabla f_\Theta(x)|) dx + \int_{x_j}^{x_{j+1}} (|\nabla f_\Theta(x_{j+1})| - |\nabla f_\Theta(x)|) dx. \end{aligned}$$

Hence we have

$$(A.19) \quad \begin{aligned} R_1 - R_2 &= \int_{x_{j-1}}^{x_j - \delta} (|\nabla f_\Theta(x_j)| - |\nabla f_\Theta(x)|) - (|\nabla f_\Theta(x_j - \delta)| - |\nabla f_\Theta(x)|) dx \\ &\quad + \int_{x_j - \delta}^{x_j} (|\nabla f_\Theta(x_j)| - |\nabla f_\Theta(x)|) - (|\nabla f_\Theta(x_{j+1})| - |\nabla f_\Theta(x)|) dx \\ &= \int_{x_{j-1}}^{x_j - \delta} (|\nabla f_\Theta(x_j)| - |\nabla f_\Theta(x_j - \delta)|) dx + \int_{x_j - \delta}^{x_j} (|\nabla f_\Theta(x_j)| - |\nabla f_\Theta(x_{j+1})|) dx. \end{aligned}$$

Since $|\nabla f_\Theta(x)|$ is non-decreasing and $\nabla^2 f_\Theta(x) \geq 0$ for $x \in [x_{j-1}, x_j]$, we have $\nabla f_\Theta(x) \geq 0$ for $x \in [x_{j-1}, x_j]$. Hence we have

$$\begin{aligned}
(A.20) \quad R_1 - R_2 &= \int_{x_{j-1}}^{x_j - \delta} (|\nabla f_\Theta(x_j)| - |\nabla f_\Theta(x_j - \delta)|) dx + \int_{x_j - \delta}^{x_j} (|\nabla f_\Theta(x_j)| - |\nabla f_\Theta(x_{j+1})|) dx \\
&= (\nabla f_\Theta(x_j) - \nabla f_\Theta(x_j - \delta))(h - \delta) + (\nabla f_\Theta(x_j) - \nabla f_\Theta(x_{j+1}))\delta \\
&= \nabla^2 f_\Theta(\eta_1)\delta(h - \delta) - \nabla^2 f_\Theta(\eta_2)h\delta,
\end{aligned}$$

where $h = x_j - x_{j-1}$, $\eta_1 \in [x_j - \delta, x_j]$, and $\eta_2 \in [x_j, x_{j+1}]$. Note that $\nabla^2 f(t_1) > \nabla^2 f(t_2) \geq 0$ for any $t_1 \in [x_{j-1}, x_j]$ and $t_2 \in [x_j, x_{j+1}]$. Hence when

$$0 < \delta < \frac{h(\nabla^2 f_\Theta(\eta_1) - \nabla^2 f_\Theta(\eta_2))}{\nabla^2 f_\Theta(\eta_1)}$$

we have $R_1 - R_2 > 0$, i.e., the truncation error of numerical integration using non-uniform partitions is less than the truncation error using uniform partitions. \blacksquare

REFERENCES

- [1] M. V. AFONSO AND J. M. R. SANCHES, *Blind inpainting using ℓ_0 and total variation regularization*, IEEE Transactions on Image Processing, 24 (2015), pp. 2239–2253.
- [2] H. K. AGGARWAL AND A. MAJUMDAR, *Hyperspectral image denoising using spatio-spectral total variation*, IEEE Geoscience and Remote Sensing Letters, 13 (2016), pp. 442–446.
- [3] I. BAYRAM AND M. E. KAMASAK, *Directional total variation*, IEEE Signal Processing Letters, 19 (2012), pp. 781–784.
- [4] A. BECK AND M. TEBOULLE, *Fast gradient-based algorithms for constrained total variation image denoising and deblurring problems*, IEEE Transactions on Image Processing, 18 (2009), pp. 2419–2434.
- [5] K. BREDIES, K. KUNISCH, AND T. POCK, *Total generalized variation*, SIAM Journal on Imaging Sciences, 3 (2010), pp. 492–526.
- [6] A. CHAMBOLLE AND T. POCK, *Learning consistent discretizations of the total variation*, SIAM Journal on Imaging Sciences, 14 (2021), pp. 778–813.
- [7] T. CHAN, A. MARQUINA, AND P. MULET, *High-order total variation-based image restoration*, SIAM Journal on Scientific Computing, 22 (2000), pp. 503–516.
- [8] T. CHAN AND C.-K. WONG, *Total variation blind deconvolution*, IEEE Transactions on Image Processing, 7 (1998), pp. 370–375.
- [9] Y. CHEN, S. LIU, AND X. WANG, *Learning continuous image representation with local implicit image function*, in 2021 IEEE/CVF Conference on Computer Vision and Pattern Recognition, 2021, pp. 8624–8634.
- [10] O. DEBALS, M. VAN BAREL, AND L. DE LATHAUWER, *Nonnegative matrix factorization using nonnegative polynomial approximations*, IEEE Signal Processing Letters, 24 (2017), pp. 948–952.
- [11] A. EL HAMIDI, M. MÉNARD, M. LUGIEZ, AND C. GHANNAM, *Weighted and extended total variation for image restoration and decomposition*, Pattern Recognition, 43 (2010), pp. 1564–1576.
- [12] M. ELAD, B. KAWAR, AND G. VAKSMAN, *Image denoising: The deep learning revolution and beyond—a survey paper*, SIAM Journal on Imaging Sciences, 16 (2023), pp. 1594–1654.
- [13] E. GIUSTI, *Minimal Surfaces and Functions of Bounded Variation*, Birkhäuser Boston, MA, 1984.
- [14] B. HASHEMI AND L. N. TREFETHEN, *Chebfun in three dimensions*, SIAM Journal on Scientific Computing, 39 (2017), pp. C341–C363.
- [15] W. HE, H. ZHANG, L. ZHANG, AND H. SHEN, *Total-variation-regularized low-rank matrix factorization for hyperspectral image restoration*, IEEE Transactions on Geoscience and Remote Sensing, 54 (2016), pp. 178–188.

[16] A. HOSSEINI, *New discretization of total variation functional for image processing tasks*, Signal Processing: Image Communication, 78 (2019), pp. 62–76.

[17] G. HUANG, X. CHEN, S. QU, M. BAI, AND Y. CHEN, *Directional total variation regularized high-resolution prestack ava inversion*, IEEE Transactions on Geoscience and Remote Sensing, 60 (2022), pp. 1–11.

[18] Y.-M. HUANG, M. K. NG, AND Y.-W. WEN, *A new total variation method for multiplicative noise removal*, SIAM Journal on Imaging Sciences, 2 (2009), pp. 20–40.

[19] L. HUO, W. CHEN, H. GE, AND M. K. NG, *Stable image reconstruction using transformed total variation minimization*, SIAM Journal on Imaging Sciences, 15 (2022), pp. 1104–1139.

[20] M. IMAIZUMI AND K. HAYASHI, *Tensor decomposition with smoothness*, in International Conference on Machine Learning, vol. 70, 2017, pp. 1597–1606.

[21] M.-D. IORDACHE, J. M. BIOCAS-DIAS, AND A. PLAZA, *Total variation spatial regularization for sparse hyperspectral unmixing*, IEEE Transactions on Geoscience and Remote Sensing, 50 (2012), pp. 4484–4502.

[22] F. JIA, S. MAO, X.-C. TAI, AND T. ZENG, *A variational model for nonuniform low-light image enhancement*, SIAM Journal on Imaging Sciences, 17 (2024), pp. 1–30.

[23] Z. JIA, M. K. NG, AND W. WANG, *Color image restoration by saturation-value total variation*, SIAM Journal on Imaging Sciences, 12 (2019), pp. 972–1000.

[24] T.-X. JIANG, T.-Z. HUANG, X.-L. ZHAO, L.-J. DENG, AND Y. WANG, *Fastderain: A novel video rain streak removal method using directional gradient priors*, IEEE Transactions on Image Processing, 28 (2019), pp. 2089–2102.

[25] N. KARGAS AND N. D. SIDIROPOULOS, *Supervised learning and canonical decomposition of multivariate functions*, IEEE Transactions on Signal Processing, 69 (2021), pp. 1097–1107.

[26] D. KINGMA AND J. BA, *Adam: A method for stochastic optimization*, in International Conference on Learning Representations, 2015.

[27] H. LEE, J. PARK, Y. CHOI, K. R. PARK, B. J. MIN, AND I. J. LEE, *Low-dose CBCT reconstruction via joint non-local total variation denoising and cubic B-spline interpolation*, Scientific Reports, 11 (2021), p. 3681.

[28] X. LI, T.-Z. HUANG, X.-L. ZHAO, T.-Y. JI, Y.-B. ZHENG, AND L.-J. DENG, *Adaptive total variation and second-order total variation-based model for low-rank tensor completion*, Numerical Algorithms, 86 (2021), p. 1–24.

[29] X. LI, Y. YE, AND X. XU, *Low-rank tensor completion with total variation for visual data inpainting*, in AAAI Conference on Artificial Intelligence, 2017, p. 2210–2216.

[30] Z. LI, T. SUN, H. WANG, AND B. WANG, *Adaptive and implicit regularization for matrix completion*, SIAM Journal on Imaging Sciences, 15 (2022), pp. 2000–2022.

[31] H. LIU, X.-C. TAI, R. KIMMEL, AND R. GLOWINSKI, *Elastica models for color image regularization*, SIAM Journal on Imaging Sciences, 16 (2023), pp. 461–500.

[32] J. LIU, Y. SUN, X. XU, AND U. S. KAMILOV, *Image restoration using total variation regularized deep image prior*, in ICASSP 2019 - 2019 IEEE International Conference on Acoustics, Speech and Signal Processing, 2019, pp. 7715–7719.

[33] T. LIU, J. YANG, B. LI, Y. WANG, AND W. AN, *Representative coefficient total variation for efficient infrared small target detection*, IEEE Transactions on Geoscience and Remote Sensing, 61 (2023), <https://doi.org/10.1109/TGRS.2023.3324821>.

[34] Y. LIU, Z. LONG, AND C. ZHU, *Image completion using low tensor tree rank and total variation minimization*, IEEE Transactions on Multimedia, 21 (2019), pp. 338–350.

[35] Y. LUO, X. ZHAO, Z. LI, M. K. NG, AND D. MENG, *Low-rank tensor function representation for multi-dimensional data recovery*, IEEE Transactions on Pattern Analysis and Machine Intelligence, (2023), <https://doi.org/10.1109/TPAMI.2023.3341688>.

[36] Y. LUO, X. ZHAO, D. MENG, AND T. JIANG, *Hlrf: Hierarchical low-rank tensor factorization for inverse problems in multi-dimensional imaging*, in 2022 IEEE/CVF Conference on Computer Vision and Pattern Recognition, 2022, pp. 19281–19290.

[37] V. MARX, *Method of the year: spatially resolved transcriptomics*, Nature Methods, 18 (2021), p. 9–14.

[38] B. MILDENHALL, P. P. SRINIVASAN, M. TANCIK, J. T. BARRON, R. RAMAMOORTHI, AND R. NG, *NeRF: Representing scenes as neural radiance fields for view synthesis*, in European Conference on Computer

Vision, 2020, pp. 405–421.

[39] M. K. NG AND W. WANG, *A total variation model for retinex*, SIAM Journal on Imaging Sciences, 4 (2011), pp. 345–365.

[40] S. PARISOTTO, J. LELLMANN, S. MASNOU, AND C.-B. SCHÖNLIEB, *Higher-order total directional variation: Imaging applications*, SIAM Journal on Imaging Sciences, 13 (2020), pp. 2063–2104.

[41] M. PRAGLIOLA, L. CALATRONI, A. LANZA, AND F. SGALLARI, *On and beyond total variation regularization in imaging: The role of space variance*, SIAM Review, 65 (2023), pp. 601–685.

[42] L. I. RUDIN, S. OSHER, AND E. FATEMI, *Nonlinear total variation based noise removal algorithms*, Physica D: Nonlinear Phenomena, 60 (1992), pp. 259–268.

[43] V. SITZMANN, J. MARTEL, A. BERGMAN, D. LINDELL, AND G. WETZSTEIN, *Implicit neural representations with periodic activation functions*, in Advances in Neural Information Processing Systems, vol. 33, 2020, pp. 7462–7473.

[44] T. SONG, C. BROADBENT, AND R. KUANG, *GNTD: reconstructing spatial transcriptomes with graph-guided neural tensor decomposition informed by spatial and functional relations*, Nature Communications, 14 (2023), p. 8276.

[45] M. TANCIK, P. SRINIVASAN, B. MILDENHALL, S. FRIDOVICH-KEIL, N. RAGHAVAN, U. SINGHAL, R. RAMAMOORTHI, J. BARRON, AND R. NG, *Fourier features let networks learn high frequency functions in low dimensional domains*, in Advances in Neural Information Processing Systems, vol. 33, 2020, pp. 7537–7547.

[46] D. ULYANOV, A. VEDALDI, AND V. LEMPITSKY, *Deep image prior*, International Journal of Computer Vision, 128 (2020), p. 1867–1888.

[47] G. WANG, J. ZHAO, Y. YAN, Y. WANG, A. R. WU, AND C. YANG, *Construction of a 3d whole organism spatial atlas by joint modeling of multiple slices*, Nature Machine Intelligence, 5 (2023), p. 1200–1213.

[48] H. WANG, J. PENG, W. QIN, J. WANG, AND D. MENG, *Guaranteed tensor recovery fused low-rankness and smoothness*, IEEE Transactions on Pattern Analysis and Machine Intelligence, 45 (2023), pp. 10990–11007.

[49] Y. WANG, J. PENG, Q. ZHAO, Y. LEUNG, X.-L. ZHAO, AND D. MENG, *Hyperspectral image restoration via total variation regularized low-rank tensor decomposition*, IEEE Journal of Selected Topics in Applied Earth Observations and Remote Sensing, 11 (2018), pp. 1227–1243.

[50] Z. XU, Y. LUO, B. WU, AND D. MENG, *S2S-WTV: Seismic data noise attenuation using weighted total variation regularized self-supervised learning*, IEEE Transactions on Geoscience and Remote Sensing, 61 (2023), pp. 1–15.

[51] F. YASUMA, T. MITSUNAGA, D. ISO, AND S. K. NAYAR, *Generalized assorted pixel camera: Postcapture control of resolution, dynamic range, and spectrum*, IEEE Transactions on Image Processing, 19 (2010), pp. 2241–2253.

[52] T. YOKOTA, R. ZDUNEK, A. CICHOCKI, AND Y. YAMASHITA, *Smooth nonnegative matrix and tensor factorizations for robust multi-way data analysis*, Signal Processing, 113 (2015), pp. 234–249.

[53] C. YU, Y. CHANG, Y. LI, X. ZHAO, AND L. YAN, *Unsupervised image deraining: Optimization model driven deep CNN*, in Proceedings of the 29th ACM International Conference on Multimedia, 2021, p. 2634–2642.

[54] Y. ZHANG, Y.-M. CHEUNG, AND W. SU, *A total-variation constrained permutation model for revealing common copy number patterns*, Scientific Reports, 7 (2017), p. 9666.

[55] X.-L. ZHAO, F. WANG, AND M. K. NG, *A new convex optimization model for multiplicative noise and blur removal*, SIAM Journal on Imaging Sciences, 7 (2014), pp. 456–475.

[56] X.-L. ZHAO, W. WANG, T.-Y. ZENG, T.-Z. HUANG, AND M. K. NG, *Total variation structured total least squares method for image restoration*, SIAM Journal on Scientific Computing, 35 (2013), pp. B1304–B1320.

[57] Y.-B. ZHENG, T.-Z. HUANG, X.-L. ZHAO, Y. CHEN, AND W. HE, *Double-factor-regularized low-rank tensor factorization for mixed noise removal in hyperspectral image*, IEEE Transactions on Geoscience and Remote Sensing, 58 (2020), pp. 8450–8464.

[58] J. ZHUANG, Y. LUO, X. ZHAO, T. JIANG, AND B. GUO, *UConNet: Unsupervised controllable network for image and video deraining*, in Proceedings of the 30th ACM International Conference on Multimedia, 2022, p. 5436–5445.

[59] J.-H. ZHUANG, Y.-S. LUO, X.-L. ZHAO, AND T.-X. JIANG, *Reconciling hand-crafted and self-supervised*

deep priors for video directional rain streaks removal, IEEE Signal Processing Letters, 28 (2021), pp. 2147–2151.

[60] J.-H. ZHUANG, Y.-S. LUO, X.-L. ZHAO, T.-X. JIANG, Y. CHANG, AND J. LIU, *Unsupervised video rain streaks removal with deep foreground–background modeling*, Journal of Computational and Applied Mathematics, 436 (2024), p. 115431.